http://pubs.acs.org/journal/aesccq

Article

High-Temperature Thermodynamics of Cerium Silicates, A-$Ce_2Si_2O_7$, and $Ce_{4.67}(SiO_4)_3O$

Andrew C. Strzelecki, Kyle Kriegsman, Paul Estevenon, Vitaliy Goncharov, Jianming Bai, Stephanie Szenknect, Adel Mesbah, Di Wu, John S. McCloy, Nicolas Dacheux, and Xiaofeng Guo*

Cite This: *ACS Earth Space Chem.* 2020, 4, 2129−2143

Read Online

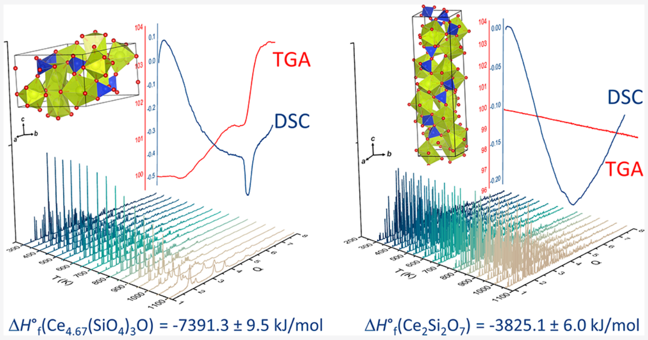

ABSTRACT: Lanthanide disilicates and oxyapatites have potential roles in high-temperature applications as thermal (TBC) and environmental barrier coatings (EBC) or possible alteration phases in geological nuclear waste repositories. However, those Ce^{3+}-bearing silicates have only been limitedly studied. In this work, we performed detailed structural and thermodynamic investigations on A-$Ce_2Si_2O_7$ (tetragonal, $P4_1$) and $Ce_{4.67}(SiO_4)_3O$ (hexagonal, $P6_3/m$). The high-temperature structural behaviors and coefficients of thermal expansion were determined by *in situ* high-temperature synchrotron X-ray diffraction (HT-XRD) implemented with Rietveld analysis and thermogravimetric analysis coupled with differential scanning calorimetry (TGA-DSC). A-$Ce_2Si_2O_7$ was found to be stable in N_2 and air up to ∼1483 K with an isotropic thermal expansion along the *a*- and *c*-axes ($\alpha_a = 12.3 \times 10^{-6}$ K^{-1} and $\alpha_c = 12.4 \times 10^{-6}$ K^{-1}). $Ce_{4.67}(SiO_4)_3O$ had a slow partial oxidation between 533 and 873 K to a new nonstoichiometric phase $Ce^{3+}{}_{1.67-x}Ce^{4+}{}_xCe^{3+}{}_3(SiO_4)_3O_{1+0.5x}$, followed by a thermal decomposition to CeO_2 and SiO_2 at ∼1000 K in air. By using high temperature oxide melt solution calorimetry at 973 K with lead borate as the solvent, the standard enthalpy of formation was determined for A-$Ce_2Si_2O_7$ (−3825.1 ± 6.0 kJ/mol) and $Ce_{4.67}(SiO_4)_3O$ (−7391.3 ± 9.5 kJ/mol). These thermodynamic parameters were compared with those of CeO_2, $CeSiO_4$, and other silicate oxyapatites for examining their chemical stability in high-temperature environments relevant for aeronautical applications, mineral formation, and nuclear fuel cycle.

KEYWORDS: *cerium sorosilicate, cerium oxyapatite, thermodynamics, enthalpy of formation, thermal barrier coating, environmental barrier coatings, ceramic waste forms, rare earth minerals, lanthanide geochemistry*

1. INTRODUCTION

Rare-earth disilicates ($RE_2Si_2O_7$) display the largest number of polymorphs of any rare-earth oxide compounds[1] and have applications as thermal (TBCs) and environmental barrier coatings (EBCs) for ceramic matrix composite materials (CMC), such as silicon carbide (SiC) or molybdenum disilicide ($MoSi_2$).[1−3] The advantages of silicate-based coating materials are their high thermal stability and resistance to oxidation, while possessing congruent coefficients of thermal expansion (CTE) with the existing high-temperature CMC (Table 1).[1,2,4−9] This makes the rare-earth disilicates attractive potential candidates to be used in high-temperature combustion engines for aerospace applications which are to replace traditional nickel-based super alloys.[2,3] However, during the takeoff and landing of aircraft, various rare-earth oxyapatites ($M^{2+}RE_4(SiO_4)_3O$) are known to form as corrosion products between the rare-earth disilicates EBC and molten aerosol mineral dust, composed primarily of $CaO-MgO-Al_2O_3-SiO_2$ (CMAS).[10,11] Such rare-earth oxyapatite corrosion products are thermodynamically stable and can serve as an effective passivating layer to reduce or prevent further pitting and erosion of EBC/CMC on the engines of the aircraft.[10,12,13] Conversely, the potential mismatch of CTEs of the rare-earth oxyapatite and the EBC/CMC could also cause increased internal stresses promoting mechanical failure.

In addition to their high-temperature properties, these rare earth silicates material families have potential applications to various other fields and technologies because of their diverse properties originating from the 4f electronic states.[14−16] Examples of such applications include use as scintillators and detectors in monitoring radionuclides;[17−19] ion-exchange medium for the separation of radionuclides due to their

Special Issue: Materials of the Universe: The Final Chemical Frontier

Received: August 25, 2020
Revised: October 6, 2020
Accepted: October 16, 2020
Published: October 30, 2020

Table 1. Summary of CTE Values for CMC and TBC/EBC Materials

category	material	CTE (10^{-6} K^{-1})	reference
CMC	Si	4.0	4
CMC	SiC	5.0	4
CMC	Si_3N_4	3.5	4
CMC	$MoSi_2$	8.5	5
TBC/EBC	Mullite	5.4	4, 6
TBC/EBC	δ-$RE_2Si_2O_7$	7.7	1, 7
TBC/EBC	γ-$RE_2Si_2O_7$	4.1	1, 7−9
TBC/EBC	β-$RE_2Si_2O_7$	4.4	1, 7, 76
TBC/EBC	α-$RE_2Si_2O_7$	8.3	1, 7
TBC/EBC	G-$RE_2Si_2O_7$	6.6	1
TBC/EBC	A-$RE_2Si_2O_7$	12.1	1
substrate of TBC	IN737 superalloy	16.0	6

efficient ability for ion exchange and robust nature;[20] and optoelectronics (lasers and optical fibers) as a result of the thermal stability of their optical transmission.[17,18,21] As a result, structural and thermochemical investigations have been detailed at both low and high temperatures.[1,2,21−27,11,14−20] However, the thermophysical and thermochemical understanding of the low temperature polymorph of cerium disilicate (A-$Ce_2Si_2O_7$; space group $P4_1$) and the cation-vacant cerium oxyapatite ($Ce_{4.67}(SiO_4)_3O$; space group $P6_3/m$) are still largely absent (Figure 1). Additionally, as Ce is the most abundant rare earth element[28] and an effective surrogate for Pu in the solid state system,[29−33] the thermodynamic properties of A-$Ce_2Si_2O_7$ and $Ce_{4.67}(SiO_4)_3O$ are fundamentally needed for geochemical modeling and are desirable to evaluate the thermodynamics of Pu in silicate solid systems.

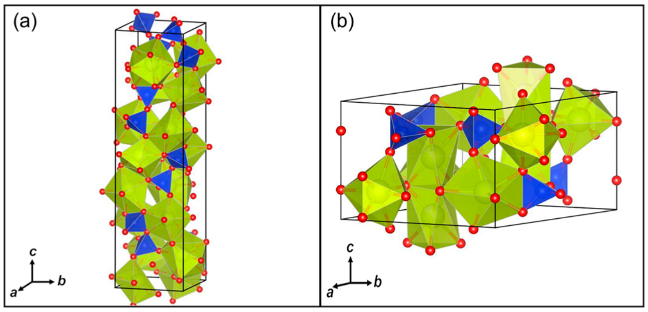

Figure 1. Structures of (a) A-$Ce_2Si_2O_7$ (space group, $P4_1$) and (b) $Ce_{4.67}(SiO_4)_3O$ (space group, $P6_3/m$).[58,59,116]

Indeed, both of the Ce(III) silicates widely exist in natural systems, industrial processing, and synthetic conditions. A-$Ce_2Si_2O_7$ is found in nature as the mineral percleveite[34] and $Ce_{4.67}(SiO_4)_3O$ in the manufacturing of steel.[26,35] $Ce_{4.67}(SiO_4)_3O$ also belongs to cation-vacant rare earth oxyapatites, an important family among the rare earth silicates, as all 17 rare earth elements (Sc, Y, La−Lu) can crystallize into this structure.[15,21] Furthermore, in the pursuit of pure cerium orthosilicate ($CeSiO_4$; space group $I4_1/amd$), a rare mineral,[36] which is isostructural to coffinite ($USiO_4$), thorite ($ThSiO_4$), and $PuSiO_4$, both A-$Ce_2Si_2O_7$ and $Ce_{4.67}(SiO_4)_3O$ were used as solid precursors during hydrothermal synthesis.[37] Such observations imply that the three Ce silicate phases could be close in energetics. A recent work published by Estevenon et al.[38] in 2020 also showed that impure $PuSiO_4$ was synthesized hydrothermally from a plutonium disilicate ($Pu_2Si_2O_7$) precursor, again suggesting the equilibrium between these silicate phases. Such a closeness in energetics could be detrimental to nuclear waste applications. In the permanent disposal of nuclear wastes, either in a deep bore-hole or mined geologic repository, elevated temperatures (343−623 K) will be encountered by the waste forms as a result of both the radiogenic heat mainly generated from the beta decay of short-lived radionuclides and also the geothermal gradient.[39−43] These elevated conditions imitate natural metasomatic conditions within hydrothermal ore deposits.[44] Radionuclides, especially actinides (An), when leaked from the multibarrier systems may interact with silicate-rich fluids. They could potentially form An-silicate colloids,[45−48] solid particles,[38,49,50] or An-silicate aqueous complexes[51,52] under either hydrothermal conditions presented in the early stages of the repository or ambient conditions in either the late stages of the repository or down the hydrogeological gradient. Such concerns are further justified as it has been previously demonstrated that Pu and other actinides can be transported on immense distances in the colloidal forms.[53−55]

Thus, studying the high-temperature thermal stability and thermodynamic properties of these two cerium silicate materials has both fundamental and applicable significance. In this work, we performed structural and calorimetric investigations on A-$Ce_2Si_2O_7$ and $Ce_{4.67}(SiO_4)_3O$ by thermogravimetric analysis coupled with differential scanning calorimetry (TGA-DSC), *in situ* high-temperature synchrotron X-ray diffraction (HT-XRD), and high temperature oxide melt drop solution calorimetry. The determined mean CTEs and enthalpies of formation (ΔH_f) enable us to further evaluate their high-temperature thermochemical reactions and thermophysical behaviors relevant to high-temperature material science applications, geochemical associations of these materials, and the nuclear fuel cycle.

2. EXPERIMENTAL METHODS

2.1. Sample Synthesis and Characterization. All of the reagents used for synthesis were of analytical grade. Both of the two cerium(III) silicates, A-$Ce_2Si_2O_7$ and $Ce_{4.67}(SiO_4)_3O$, were prepared via solid state synthetic techniques. This involved mixing of well-milled CeO_2 (99.5%) and SiO_2 (99.5%) in a stoichiometric proportion to the target materials, then pelletizing the homogeneous powder under 5 MPa at room temperature. Following this, the pelletized samples were heated to 1623 K for 9 h under Ar−H_2 4% atmosphere in order to guarantee the reduction of cerium. Thorough phase identification was accomplished by powder X-ray diffraction (PXRD), Raman spectroscopy, and infrared spectroscopy. A more detailed description of the synthesis procedure and characterization techniques is described in the previously published work.[37]

2.2. Thermogravimetric Analysis Coupled with Differential Scanning Calorimetry (TGA-DSC). The TGA-DSC measurements were performed on a Setaram SetSYS thermogravimetric differential scanning calorimeter, where $Ce_{4.67}(SiO_4)_3O$ and A-$Ce_2Si_2O_7$ were heated from 301 to 1473 K and from 301 to 1673 K, respectively, with a heating rate of 10 K/min under a flowing N_2 atmosphere (20 mL/min). In addition, each compound was also heated from 301 to 1273 K with a heating rate of 10 K/min under a flowing standard air atmosphere (20 mL/min). The temperature and sensitivity of the instrument were calibrated by heating indium, tin, lead, zinc, and aluminum across their fusion point repeatedly at the temperature change rates of 5, 10, 15, and 20 K/min. The signal of each phase transition was then calibrated against the known heats of fusion for the metals.

2.3. *In Situ* High-Temperature Powder X-ray Diffraction (HT-PXRD). *In situ* HT-PXRD was conducted at the Sector 28-ID-2 of National Synchrotron Light Source-II (NSLS-II) at Brookhaven National Laboratory. The wavelength of the X-ray beam was 0.1949 Å (63.6 keV) with a beam size of 0.60 × 0.20 mm. A-$Ce_2Si_2O_7$ and $Ce_{4.67}(SiO_4)_3O$ powders were contained in a silica glass capillary (1 mm ID, 0.25 mm thickness) with one side opened to the air. The capillary was then inserted into a custom-built Kanthal coil-based furnace under standard atmosphere for heating and cooling. A K-type thermocouple was mounted near the center of the heating coil and was used to monitor and to control the temperature. The sample temperature was calibrated by measuring the CTE of a standard ceria powder at different temperature points with a heating rate of 20 K/min. The data was collected every 50 K during heating from room temperature up to 1052 K and every 200 K during cooling. Approximately 3 min of idle time was achieved between reaching the temperature points and data collection in order to establish thermal equilibrium. All collected two-dimensional (2D) images were calibrated, masked, and integrated through the use of Dioptas processing software.[56] The obtained XRD patterns were then analyzed through the Rietveld method using General Structure Analysis System software version II (GSAS-II),[57] where the instrument parameters were obtained using the CeO_2 standard. The backgrounds of A-$Ce_2Si_2O_7$ and $Ce_{4.67}(SiO_4)_3O$ were modeled by the Chebyshev function with 12 coefficients. The starting point of the refinements was the structure reported by Deng and Ibers[58] for A-$Ce_2Si_2O_7$ and the structure reported by Belokoneva et al.[59] for $Ce_{4.67}(SiO_4)_3O$. The resulting refinements yielded R_{wp} values ranging from 2.18 to 5.38% for A-$Ce_2Si_2O_7$ and 3.92 to 8.58% for $Ce_{4.67}(SiO_4)_3O$. Representative patterns resulting from the fitting are shown in Figures 2 and 3 for A-$Ce_2Si_2O_7$ and $Ce_{4.67}(SiO_4)_3O$, respectively. The refined unit cell parameters of A-$Ce_2Si_2O_7$ and $Ce_{4.67}(SiO_4)_3O$ are listed in Tables 2 and 3 and exhibited in Figures 4 and 5, respectively.

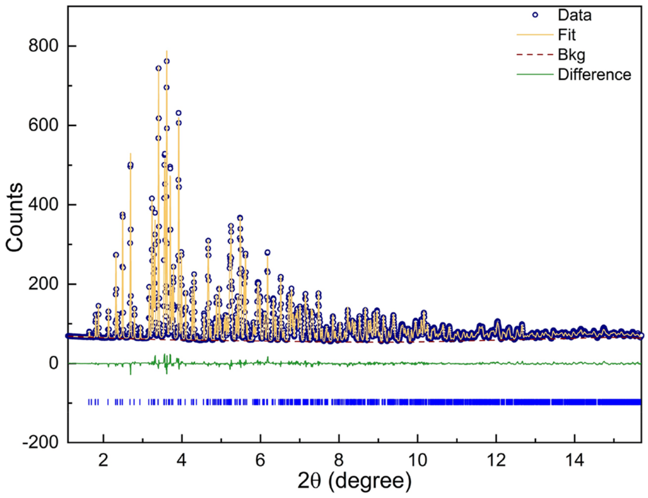

Figure 2. Fitted synchrotron XRD patterns of A-$Ce_2Si_2O_7$ collected at 301 K. Data are shown as blue circles and the solid yellow curve is the best fit obtained from the data. The green dashed curve represents the difference between the observed and calculated profiles. The blue tick marks above the *x*-axis indicate the positions of allowed diffraction maxima.

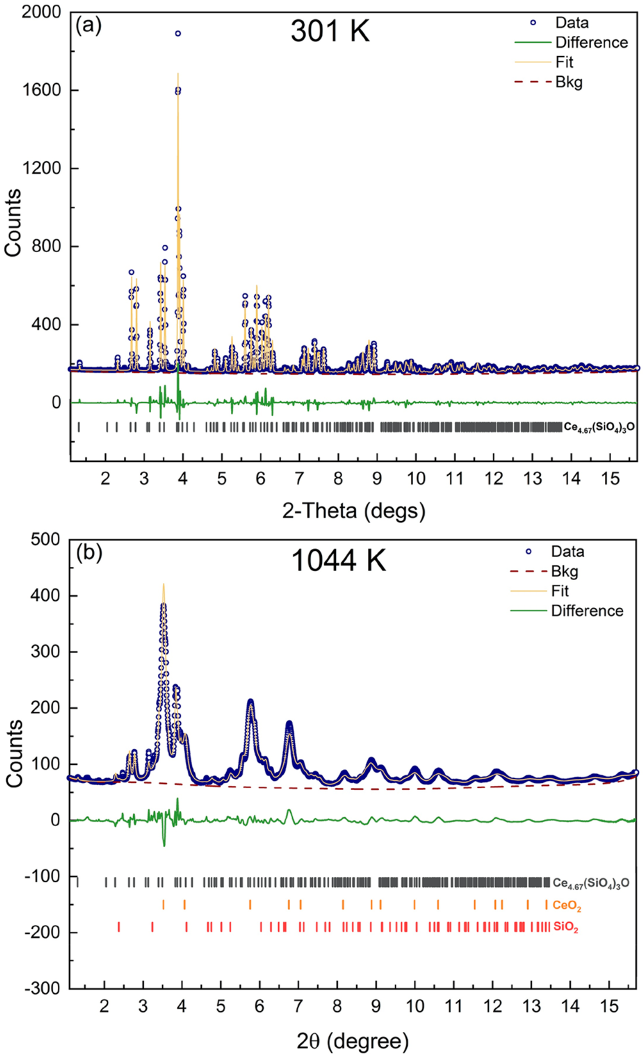

Figure 3. Fitted synchrotron XRD patterns of $Ce_{4.67}(SiO_4)_3O$ at (a) 301 K and (b) 1044 K. Data are shown as blue circles. The solid yellow curve is the best fit to the data. The green dashed curve represents the difference between the observed and calculated profiles. The tick marks above the *x*-axis indicate the positions of allowed diffraction maxima for $Ce_{4.67}(SiO_4)_3O$ (gray), CeO_2 (orange), and SiO_2 (red).

2.4. High Temperature Oxide Melt Drop Solution Calorimetry. The enthalpies of drop solution (ΔH_{ds}) were directly measured by a Setaram AlexSYS-1000 Calvet-type calorimeter. The calibration of the instrument was conducted by performing transpose temperature drops using solid pieces of α-Al_2O_3 (36−50 mg) and Pt (160−230 mg). Powdered samples were hand-pressed into pellets with a mass of 3.5−6.6 mg, and dropped from room temperature into a molten solvent of lead borate ($2PbO\cdot B_2O_3$) contained in a Pt crucible at 973 K under flowing compressed air with a rate of 100 mL/min. Although it is known that the sodium molybdate ($3Na_2O\cdot 4MoO_3$) solvent can readily dissolve lanthanides better than $PbO\cdot B_2O_3$ at 973 K, it is chemically inert to Si.[60] Therefore, the lead borate solvent was chosen to be used in this work. All of the calibration and methodology employed in this study are described previously in more detail.[60−66]

Table 2. Summary of Unit Cell Parameters and Refinement Agreements for A-$Ce_2Si_2O_7$

temperature (K)	a (Å)	c (Å)	volume (Å^3)	R_{wp} (%)
301	6.79901(7)	24.7346(2)	1143.40(2)	2.18
357	6.80225(7)	24.7469(2)	1145.05(2)	2.21
411	6.80677(9)	24.7633(2)	1147.34(3)	2.65
460	6.8104(1)	24.7772(2)	1149.19(3)	2.91
512	6.8147(1)	24.7929(2)	1151.40(3)	3.00
553	6.8187(1)	24.8065(3)	1153.38(4)	3.14
611	6.8231(1)	24.8232(3)	1155.64(4)	3.29
671	6.8284(1)	24.8439(3)	1158.41(5)	3.88
704	6.8327(2)	24.8595(4)	1160.60(5)	4.05
787	6.8365(2)	24.8729(4)	1162.52(5)	4.27
816	6.8410(2)	24.8901(4)	1164.85(6)	4.75
868	6.8452(2)	24.9057(5)	1166.99(6)	4.95
911	6.8488(2)	24.9191(5)	1168.85(6)	4.94
956	6.8528(2)	24.9336(5)	1170.90(7)	5.06
1001	6.8565(2)	24.9471(5)	1172.78(7)	5.22
1052	6.8599(2)	24.9591(5)	1174.53(7)	5.38

Table 3. Summary of Unit Cell Parameters, Refinement Agreements, and Values for x for $^{XI}Ce^{3+}_{1.67-x}{}^{IX}Ce^{4+}_{x}{}^{VII}Ce^{3+}_{3}(^{IV}Si^{IV}O_4)_3{}^{III}O_{1+0.5x}$ ($0 < x < 0.27$)

temperature (K)	a (Å)	c (Å)	volume (Å^3)	R_{wp} (%)	x
301	9.6562(7)	7.0933(2)	572.78(5)	7.18	0.00
356	9.6604(7)	7.0956(2)	573.47(5)	7.07	0.00
408	9.6640(7)	7.0981(2)	574.10(5)	6.96	0.00
459	9.6664(6)	7.0994(2)	574.49(4)	6.80	0.00
513	9.6724(6)	7.1026(1)	575.46(4)	6.43	0.00
559	9.6776(6)	7.1023(1)	576.05(4)	5.92	0.04
617	9.6797(6)	7.0927(1)	575.53(4)	5.91	0.08
668	9.6864(6)	7.0841(2)	575.62(4)	6.05	0.11
717	9.6965(7)	7.0835(2)	576.78(5)	6.13	0.15
762	9.7089(8)	7.0871(2)	578.55(6)	6.45	0.18
818	9.720(1)	7.0879(2)	579.97(7)	6.84	0.23
863	9.739(1)	7.0928(3)	582.6(1)	7.28	0.26
907	9.749(2)	7.0936(4)	583.9(1)	7.84	0.27
954	9.767(3)	7.1004(6)	586.6(2)	8.58	0.27

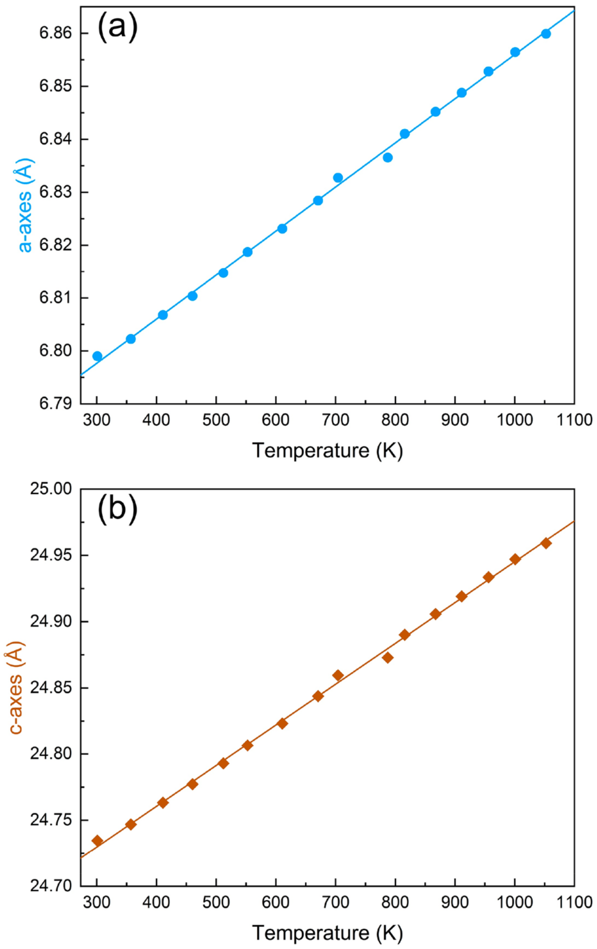

Figure 4. Variation of the unit cell parameters of A-$Ce_2Si_2O_7$ as a function of temperature. The equation of the line for (a) is a (Å) = $(6.7726 \pm 0.0006) + (8.33 \pm 0.08) \times 10^{-5} \times x$ (with $R^2 = 0.998$) and for (b) is c (Å) = $(24.637 \pm 0.002) + (3.08 \pm 0.03) \times 10^{-4} \times x$ (with $R^2 = 0.998$).

3. RESULTS

3.1. Thermogravimetric Analysis Coupled with Differential Thermal Analysis (TGA-DSC).

From the TGA-DSC result under an inert N_2 atmosphere, A-$Ce_2Si_2O_7$ showed no apparent mass loss over the entire temperature regime (301−1673 K, Figure 6). However, a change in the heat flow was observed from 1483 to 1583 K. This change in the heat flow was interpreted as the isochemical phase change from the low-temperature tetragonal, $P4_1$, A-phase to the high-temperature monoclinic, $P2_1/n$, G-phase.[27,37,67] Such a transition involves the reconstruction of the coordination polyhedra through breaking of the cerium−oxygen bonds[16] and is consistent with previously reported findings of being a "sluggish" transition from 1523 to 1548 K.[27,67] The TGA-DSC result of $Ce_{4.67}(SiO_4)_3O$ exhibited no mass loss or phase transition from 301 to 1473 K (Figure 7), which is also in good agreement with the previous study showing that $Ce_{4.67}(SiO_4)_3O$ was found to be stable under N_2 atmosphere up to its melting point of 2143 K.[27]

Under an oxidative atmosphere (synthetic air), A-$Ce_2Si_2O_7$ had a similar thermal stability (Figure 8) with no signs of degradation or polymorphism, while $Ce_{4.67}(SiO_4)_3O$ was found to be unstable, as suggested by two weight gains (Figure 9). The first mass gain of 1.66% occurred from 533 to 923 K. It was associated with the oxidation of Ce^{3+} to Ce^{4+}, resulting in a cerium oxyapatite of mixed-valence states with a proposed chemical formula $Ce^{3+}_{1.67-x}Ce^{4+}_{x}Ce^{3+}_{3}(SiO_4)_3O_{1+0.5x}$. The second mass gain of 2.10% occurred between 973 and 1123 K. It was attributed to the decomposition of $Ce^{3+}_{1.67-x}Ce^{4+}_{x}Ce^{3+}_{3}(SiO_4)_3O_{1+0.5x}$ into its binary oxides, SiO_2 and CeO_2. These conclusions are further supported by the following HT-XRD results as reported below.

3.2. *In Situ* High-Temperature X-ray Diffraction (HT-XRD) of A-$Ce_2Si_2O_7$.

Figure S1 shows the temperature-dependent XRD patterns of A-$Ce_2Si_2O_7$ in the temperature range between 301 and 1052 K in air atmosphere. The absence of phase decomposition or transition was consistent with our TGA-DSC experiment performed in the air (Figure 8) and previous studies.[27,37,67] Rietveld analysis of the XRD data determined the variation of the unit cell parameters as a function of temperature. The linear regressions of such data along both the a-axes and the c-axes (Figure 4) yielded

$$301{-}1052\ \text{K} \quad a\ (\text{Å}) = 6.7727 + 8.32 \times 10^{-5}T\ (\text{K}) \quad R^2 = 0.998 \tag{1}$$

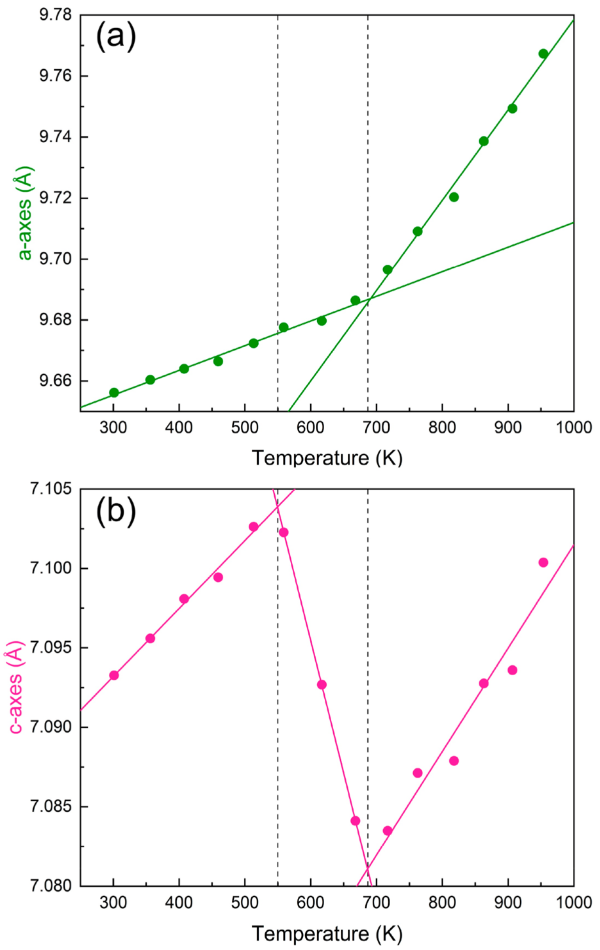

Figure 5. Unit cell parameters as a function of temperature for $Ce_{4.67}(SiO_4)_3O$. (a) The equation of the line describing the variation of a is a (Å) = $(9.631 \pm 0.002) + (8.1 \pm 0.4) \times 10^{-5} \times x$ between 301 and 668 K (with $R^2 = 0.986$), a (Å) = $(9.48 \pm 0.01) + (3.0 \pm 0.1) \times 10^{-5} \times x$ between 717 and 953 K (with $R^2 = 0.989$); (b) c (Å) = $(7.080 \pm 0.001) + (4.3 \pm 0.2) \times 10^{-5} \times x$ between 301 and 513 K (with $R^2 = 0.987$), c (Å) = $(7.1954 \pm 0.0005) - (16.66 \pm 0.08) \times 10^{-5} \times x$ (with $R^2 = 0.999$) between 559 and 668 K, and c (Å) = $(7.035 \pm 0.007) + (6.5 \pm 0.9) \times 10^{-5} \times x$ (with $R^2 = 0.920$) between 717 and 953 K.

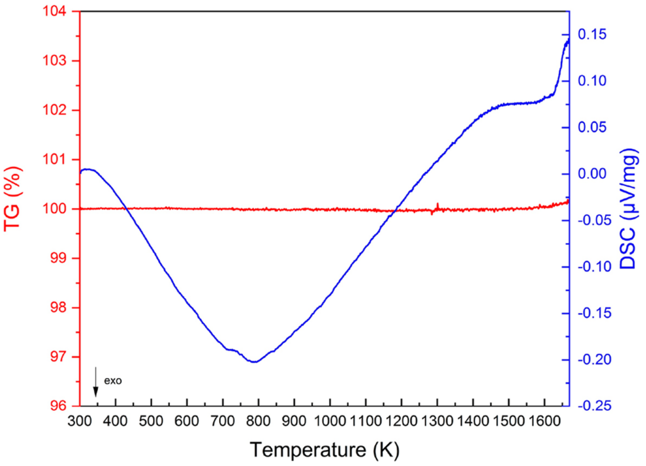

Figure 6. TGA-DSC of A-$Ce_2Si_2O_7$ under a N_2 atmosphere (starting sample mass of 7.655 mg).

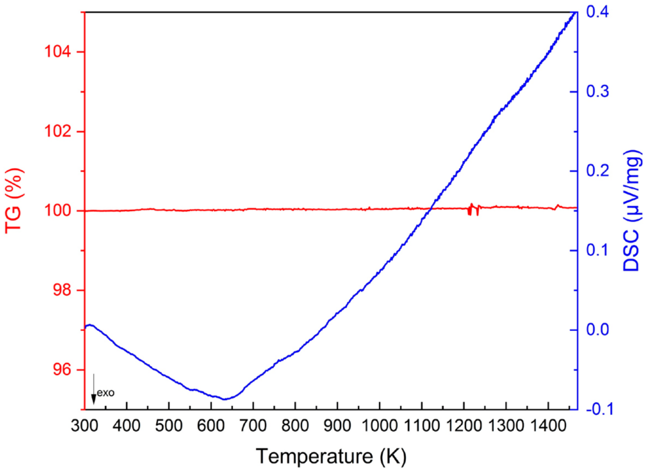

Figure 7. TGA-DSC of $Ce_{4.67}(SiO_4)_3O$ under a N_2 atmosphere (starting sample mass of 4.885 mg).

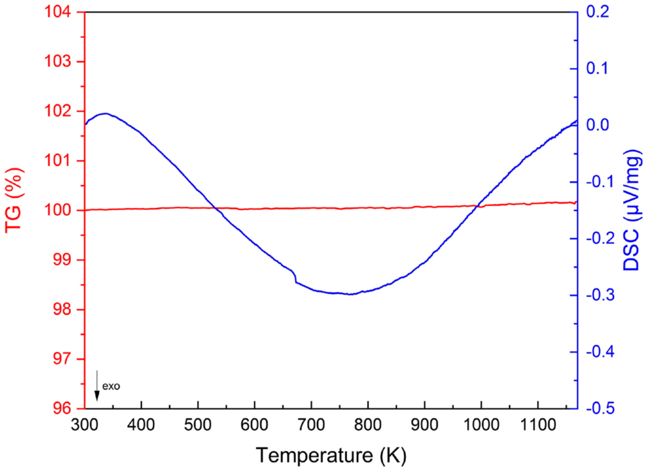

Figure 8. TGA-DSC of A-$Ce_2Si_2O_7$ under a synthetic air atmosphere (starting sample mass of 4.345 mg).

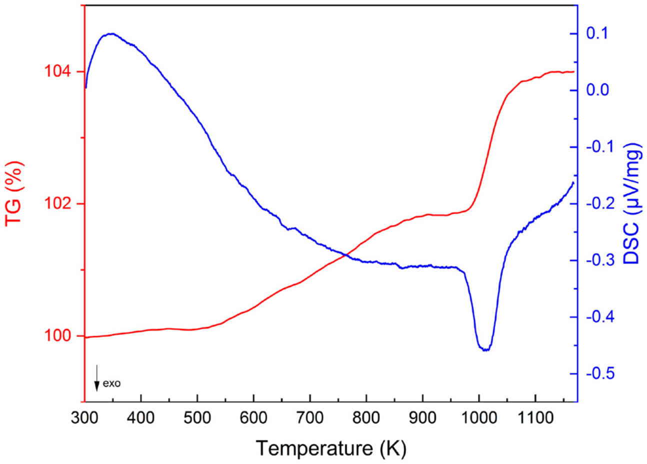

Figure 9. TGA-DSC of $Ce_{4.67}(SiO_4)_3O$ under a synthetic air atmosphere (starting sample mass of 1.901 mg).

$$301{-}1052\ \text{K}\qquad c\ (\text{Å}) = 24.637 + 30.7 \times 10^{-5}T\ (\text{K})\qquad R^2 = 0.998 \tag{2}$$

The derived mean CTEs of A-$Ce_2Si_2O_7$ are $\alpha_a = 12.3 \times 10^{-6}$ K^{-1} and $\alpha_c = 12.4 \times 10^{-6}$ K^{-1}, demonstrating that A-$Ce_2Si_2O_7$

Table 4. Thermochemical Cycles Used for Calculations of the Enthalpy of Formation from Binary Oxides and the Standard Enthalpy of Formation of Percleveite Based on the Data of Drop Solution Calorimetry in Molten Lead Borate at 973 K

reaction	ΔH (kJ/mol)
(1) $Ce_2Si_2O_{7(s,\ 298\ K)} + 0.5O_{2(g,\ 973\ K)} \rightarrow 2CeO_{2(sln,973\ K)} + 2SiO_{2(sln,\ 973\ K)}$	$\Delta H_1 = 140.05$[a] $\pm$ 3.98[b] (5)[c]
(2) $CeO_{2(s,\ 298\ K)} \rightarrow CeO_{2(sln,\ 973\ K)}$	$\Delta H_2 = 122.9 \pm 2.6$[30]
(3) $SiO_{2(quartz,\ 298\ K)} \rightarrow SiO_{2(sln,\ 973\ K)}$	$\Delta H_3 = 39.4 \pm 0.4$[60]
(4) $O_{2(g,\ 298\ K)} \rightarrow O_{2(g,\ 973\ K)}$	$\Delta H_4 = 21.74 \pm 0.02$[88]
(5) $Ce_{(s,\ 298\ K)} + O_{2(g,\ 298\ K)} \rightarrow CeO_{2(s,\ 298\ K)}$	$\Delta H_5 = -1088.7 \pm 1.5$[88]
(6) $Si_{(s,\ 298\ K)} + O_{2(g,\ 298\ K)} \rightarrow SiO_{2(quartz,\ 298\ K)}$	$\Delta H_6 = -910.7 \pm 1.0$[88]
(7) $2CeO_{2(s,\ 298\ K)} \rightarrow Ce_2O_{3(s,\ 298\ K)} + 0.5O_{2(g,\ 298\ K)}$	$\Delta H_7 = 371.6 \pm 5.0$
(8) $2Ce_{(s,\ 298\ K)} + 1.5O_{2(s,\ 298\ K)} \rightarrow Ce_2O_{3(s,\ 298\ K)}$	$\Delta H_8 = -1805.8 \pm 5.8$
enthalpy of formation from oxides of percleveite from CeO_2:	
$2CeO_{2(s,\ 298\ K)} + 2SiO_{2(quartz,\ 298\ K)} \rightarrow Ce_2Si_2O_{7(s,\ 298\ K)} + 0.5O_{2(g,\ 298\ K)}$	
$\Delta H_{f,ox}(Ce_2Si_2O_7) = -\Delta H(1) + 2\Delta H_2 + 2\Delta H_3 - 0.5\Delta H_4 = 173.7 \pm 5.5$ kJ/mol	
standard enthalpy of formation of percleveite from CeO_2:	
$2Ce_{(s,\ 298\ K)} + 2Si_{(s,\ 298\ K)} + 3.5O_{2(g,\ 298\ K)} \rightarrow Ce_2Si_2O_{7(s,\ 298\ K)}$	
$\Delta H^{\circ}_{f}(Ce_2Si_2O_7) = \Delta H_{f,\ ox}(Ce_2Si_2O_7) + 2\Delta H_5 + 2\Delta H_6 = -3825.1 \pm 6.0$ kJ/mol	
standard enthalpy of formation of percleveite from CeO_2 normalized to 1 mol Ce:	
$\Delta H^{\circ}_{f}(CeSiO_{3.5}) = -1912.6 \pm 3.0$ kJ/mol	
enthalpy of formation from oxides of percleveite from Ce_2O_3:	
$Ce_2O_{3(s,\ 298\ K)} + SiO_{2(quartz,\ 298\ K)} \rightarrow Ce_2Si_2O_{7(s,\ 298\ K)}$	
$\Delta H_{f,ox}(Ce_2Si_2O_7) = -\Delta H_1 + 2\Delta H_2 + 2\Delta H_3 - 0.5\Delta H_4 - \Delta H_7 = -197.9 \pm 7.4$ kJ/mol	
standard enthalpy of formation of percleveite from Ce_2O_3:	
$2Ce_{(s,\ 298\ K)} + 2Si_{(s,\ 298\ K)} + 3.5O_{2(g,\ 298\ K)} \rightarrow Ce_2Si_2O_{7(s,\ 298\ K)}$	
$\Delta H^{\circ}_{f}(Ce_2Si_2O_7) = \Delta H_{f,\ ox}(Ce_2Si_2O_7) + 2\Delta H_6 + \Delta H_8 = -3825.1 \pm 9.5$ kJ/mol	
standard enthalpy of formation of percleveite from Ce_2O_3normalized to 1 mol Ce:	
$\Delta H^{\circ}_{f}(CeSiO_{3.5}) = -1912.6 \pm 4.8$ kJ/mol	

[a]Average. [b]Two standard deviations of the average value. [c]Number of measurements.

unit cell parameters show an isotropic thermal expansion (α_c/α_a = 1.01). This isotropic behavior is consistent with the thermal behavior of an isostructural sorosilicate, A-$Nd_2Si_2O_7$.[1]

3.3. In Situ High-Temperature X-ray Diffraction (HT-XRD) of $Ce_{4.67}(SiO_4)_3O$.

The Rietveld refinement of HT-XRD data of $Ce_{4.67}(SiO_4)_3O$ (Figure S2) are in excellent agreement with the TGA-DSC analysis under standard air atmosphere. Above 1004 K, $Ce_{4.67}(SiO_4)_3O$ decomposed into a mixture of CeO_2 and SiO_2 (Figures 5b and S2), corresponding to the second mass gain from 973 to 1073 K found in the TGA-DSC analysis (Figure 9). Between 559 and 668 K, although there was no obvious structural change from space group $P6_3/m$, the parameter c displayed a negative thermal expansion (Figure 5), which was discontinued from those before 559 K and after 668 K. This can be attributed to the gradual oxidation of Ce^{3+} (1.196 Å)[68] to the smaller Ce^{4+} (1.01 Å) in the nine-coordination environment by incorporating additional "free oxygen"[21] in the special positions (0, 0, 1/4) and (0, 0, 3/4). This led to an increasing Ce^{4+} content in a chemically changing and nonstoichiometric phase of $Ce^{3+}_{1.67\text{-}x}Ce^{4+}_{x}Ce^{3+}_{3}(SiO_4)_3O_{1+0.5x}$ ($0 < x < 0.27$). Specifically, $Ce_{4.67}(SiO_4)_3O$ possesses two CeO_9 face-sharing polyhedra along the c-axis in the unit cell, which is mainly impacted by the reduction in size from Ce^{3+} to Ce^{4+} by ~15%. An overall shrinkage along the CeO_9 polyhedral chains was found to be 0.14% at 559 K, which corresponded to approximately 1% of Ce atoms being oxidized. The lattice expansion along the a-axis was nearly linear with a break in the slope occurring around 717 K. It is also coincident with changes in the unit cell along the c-axis, suggesting the thermal expansion of the new unit cell after the oxidation-driven shrinkage. Such a slow oxidation event is again consistent with the TGA-DSC experiments, which showed a mass gain of 1.66% from 533 to 923 K accompanying the broad exothermic DSC peak.

The CTEs (α_a and α_c) of $Ce_{4.67}(SiO_4)_3O$ were determined by fitting the lattice expansion as a function of temperature. Along the a-axis, two linear trends were established

$$301\text{–}668\ \text{K} \quad a\ (\text{Å}) = 9.631 + 8.1 \times 10^{-5}T\ (\text{K}) \quad R^2 = 0.986 \tag{3}$$

$$717\text{–}953\ \text{K} \quad a\ (\text{Å}) = 9.48 + 3.0 \times 10^{-4}T\ (\text{K}) \quad R^2 = 0.989 \tag{4}$$

From these equations, we derived CTE values of the a-axis to be 8.4×10^{-6} K^{-1} and 3.1×10^{-5} K^{-1} from 301 to 668 K and from 717 to 953 K, respectively. The α_a found at high temperatures was thus 3.7 times higher than that before 668 K. Such an increase in the expansion rate could be attributed to the presence of additional oxygen in the coordinates of (0, 0, 1/4) and (0, 0, 3/4). The reason why the rate of expansion did not directly coincide with the additional "free oxygens" starting at 559 K and being delayed until after 717 K could be due to the competition caused by the contraction of the c-axis occurring over this temperature interval (Figure 5). In addition, the unit cell parameter c was fitted according to three linear relations

$$301\text{–}513\ \text{K} \quad c\ (\text{Å}) = 7.080 + 4.3 \times 10^{-5}T\ (\text{K}) \quad R^2 = 0.987 \tag{5}$$

$$559\text{–}668\ \text{K} \quad c\ (\text{Å}) = 7.195 - 16.7 \times 10^{-5}T\ (\text{K}) \quad R^2 = 0.999 \tag{6}$$

$$717\text{–}953\ \text{K} \quad c\ (\text{Å}) = 7.035 + 6.5 \times 10^{-5}T\ (\text{K}) \quad R^2 = 0.920 \tag{7}$$

from which α_c values were derived as 6.0×10^{-6} K^{-1}, -23.5×10^{-6} K^{-1}, and 9.2×10^{-6} K^{-1} for 301–513 K, 559–668 K, and 717–953 K, respectively. The ratio of axial CTEs α_a/α_c varies from 1.4 to 3.4, suggesting an anisotropic behavior of $Ce_{4.67}(SiO_4)_3O$ and of $Ce^{3+}_{1.67\text{-}x}Ce^{4+}_{x}Ce^{3+}_{3}(SiO_4)_3O_{1+0.5x}$.

Table 5. Thermochemical Cycles Used for Calculations of the Enthalpy of Formation from Binary Oxides and the Standard Enthalpy of Formation of Cerium Oxyapatite Based on the Data of Drop Solution Calorimetry in Molten Lead Borate at 973 K

reaction	ΔH (kJ/mol)
(1) $Ce_{4.67}(SiO_4)_3O_{(s,\ 298\ K)} + 1.17O_{2(g,\ 973\ K)} \rightarrow 4.67CeO_{2(sln,973\ K)} + 3SiO_{2(sln,\ 973\ K)}$	$\Delta H_1 = 244.92 \pm 6.66$ (4)
(2) $CeO_{2(s,\ 298\ K)} \rightarrow CeO_{2(sln,\ 973\ K)}$	$\Delta H_2 = 122.9 \pm 2.6$[30]
(3) $SiO_{2(quartz,\ 298\ K)} \rightarrow SiO_{2(sln,\ 973\ K)}$	$\Delta H_3 = 39.4 \pm 0.4$[60]
(4) $O_{2(g,\ 298\ K)} \rightarrow O_{2(g,\ 973\ K)}$	$\Delta H_4 = 21.74 \pm 0.02$[88]
(5) $Ce_{(s,\ 298\ K)} + O_{2(g,\ 298\ K)} \rightarrow CeO_{2(s,\ 298\ K)}$	$\Delta H_5 = -1088.7 \pm 1.5$[88]
(6) $Si_{(s,\ 298\ K)} + O_{2(g,\ 298\ K)} \rightarrow SiO_{2(quartz,\ 298\ K)}$	$\Delta H_6 = -910.7 \pm 1.0$[88]
(7) $2CeO_{2(s,\ 298\ K)} \rightarrow Ce_2O_{3(s,\ 298\ K)} + 0.5O_{2(g,\ 298\ K)}$	$\Delta H_7 = 371.6 \pm 5.0$
(8) $2Ce_{(s,\ 298\ K)} + 1.5O_{2(s,\ 298\ K)} \rightarrow Ce_2O_{3(s,\ 298\ K)}$	$\Delta H_8 = -1805.8 \pm 5.8$
enthalpy of formation from oxides of cerium oxyapatite from CeO_2:	
$4.67CeO_{2(s,\ 298\ K)} + 3SiO_{2(quartz,\ 298\ K)} \rightarrow Ce_{4.67}(SiO_4)_3O_{(s,\ 298\ K)} + 1.17O_{2(g,\ 298\ K)}$	
$\Delta H_{f,ox}(Ce_{4.67}(SiO_4)_3O) = -\Delta H_1 + 4.67\Delta H_2 + 3\Delta H_3 - 1.17\ \Delta H_4 = 421.4 \pm 8.7$ kJ/mol	
Standard enthalpy of formation of cerium oxyapatite from CeO_2:	
$4.67Ce_{(s,\ 298\ K)} + 3Si_{(s,\ 298\ K)} + 6.5O_{2(g,\ 298\ K)} \rightarrow Ce_{4.67}(SiO_4)_3O_{(s,\ 298\ K)}$	
$\Delta H^{\circ}_f(Ce_{4.67}(SiO_4)_3O) = \Delta H_{f,\ ox}(Ce_{4.67}(SiO_4)_3O) + 4.67\Delta H_5 + 3\Delta H_6 = -7391.3 \pm 9.5$ kJ/mol	
standard enthalpy of formation of cerium oxyapatite from CeO_2normalized to 1 mol Ce:	
$\Delta H^{\circ}_f(CeSi_{0.64}O_{2.78}) = -1582.7 \pm 2.0$ kJ/mol	
enthalpy of formation from oxides of cerium oxyapatite from Ce_2O_3:	
$2.33Ce_2O_{3(s,\ 298\ K)} + 3SiO_{2(quartz,\ 298\ K)} \rightarrow Ce_{4.67}(SiO_4)_3O_{(s,\ 298\ K)}$	
$\Delta H_{f,ox}(Ce_{4.67}(SiO_4)_3O) = -\Delta H_1 + 4.67\Delta H_2 + 3\Delta H_3 - 1.17\Delta H_4 - 2.33\Delta H_7 = -445.6 \pm 11.6$ kJ/mol	
standard enthalpy of formation of cerium oxyapatite from Ce_2O_3:	
$4.67Ce_{(s,\ 298\ K)} + 2Si_{(s,\ 298\ K)} + 6.5O_{2(g,\ 298\ K)} \rightarrow Ce_{4.67}(SiO_4)_3O_{(s,\ 298\ K)}$	
$\Delta H^{\circ}_f(Ce_{4.67}(SiO_4)_3O) = \Delta H_{f,\ ox}(Ce_{4.67}(SiO_4)_3O) + 3\Delta H_6 + 4.67\Delta H_8 = -7391.3 \pm 14.7$ kJ/mol	
standard enthalpy of formation of cerium oxyapatite from Ce_2O_3normalized to 1 mol Ce:	
$\Delta H^{\circ}_f(CeSi_{0.64}O_{2.78}) = -1582.7 \pm 2.1$ kJ/mol	

3.4. High Temperature Oxide Melt Drop Solution Calorimetry.

The enthalpy of formation (ΔH_f) and enthalpy of formation from oxides ($\Delta H_{f,\ ox}$) were determined for A-$Ce_2Si_2O_7$ and $Ce_{4.67}(SiO_4)_3O$ by conducting high temperature oxide melt drop solution calorimetry in $PbO{\cdot}B_2O_3$ solvent. Previously, the $PbO{\cdot}B_2O_3$ solvent has been commonly used to dissolve silicate minerals,[60] including several different compositional types of rare-earth oxyapatites.[23,69,70] We also tested the solvent on $CeSiO_4$ for dissolution prior to its use to dissolve the two Ce silicates. The obtained enthalpy of drop solution (ΔH_{ds}) of $CeSiO_4$ was found to be 133.64 kJ/mol, from which we derived $\Delta H_{f,\ ox} = 28.7$ kJ/mol and $\Delta H_f = -1970.7$ kJ/mol using the thermochemical cycle reported in Table S1. Both values are in excellent agreement with the previously reported enthalpies determined for $CeSiO_4$ using $3Na_2O{\cdot}4MoO_3$ solvent ($\Delta H_{f,\ ox} = 27.5 \pm 3.1$ kJ/mol and $\Delta H_f = -1971.9 \pm 3.6$ kJ/mol).[33] Henceforth, we confirmed the complete dissolution of cerium silicate materials in the $PbO{\cdot}B_2O_3$ solvent.

The values of ΔH_{ds} were measured to be 140.05 ± 3.98 and 244.92 ± 6.66 kJ/mol for A-$Ce_2Si_2O_7$ and $Ce_{4.67}(SiO_4)_3O$, respectively. In order to derive their enthalpies of formation, we constructed two independent thermochemical cycles (shown in Tables 4 and 5) for each phase to check the data integrity and accuracy. The first one involved CeO_2 as the reference oxide whereas the second one used Ce_2O_3. The corresponding reactions of formation of A-$Ce_2Si_2O_7$ from these two different binary oxides were

$$2CeO_{2(s,298K)} + 2SiO_{2(s,298K)} \rightarrow Ce_2Si_2O_{7(s,298K)} + 0.5O_{2(g,298K)} \tag{8}$$

$$Ce_2O_{3(s,298K)} + 2SiO_{2(s,298K)} \rightarrow Ce_2Si_2O_{7(s,298K)} \tag{9}$$

Using the thermochemical cycle reported in Table 4, the enthalpies of reactions (eqs 8 and 9) were derived to be $\Delta H_{f,ox} = 173.7 \pm 5.5$ and -197.9 ± 7.4 kJ/mol, respectively. Consequently, the ΔH_f values associated with A-$Ce_2Si_2O_7$ were determined to be −3825.1 ± 6.0 and −3825.1 ± 9.5 kJ/mol. The two derived ΔH_f values were found to be identical within the experimental error, confirming the high data quality. Previously, ΔH_f of monoclinic G-$Ce_2Si_2O_7$ was determined by acid calorimetry to be −3807.6 ± 4.5 kJ/mol.[67] So the enthalpy of transition for A-$Ce_2Si_2O_7$ → G-$Ce_2Si_2O_7$ is 17.5 ± 7.5 kJ/mol, which is endothermic and needs energy to trigger such "sluggish" reconstructive transition[16] from the low-temperature tetragonal A-phase to the high-temperature monoclinic G-phase. We applied the same aforementioned calorimetric method to the following two reactions forming $Ce_{4.67}(SiO_4)_3O$

$$4.67CeO_{2(s,298K)} + 3SiO_{2(quartz,298K)} \rightarrow Ce_{4.67}(SiO_4)_3O_{(s,298K)} + 1.17O_{2(g,298K)} \tag{10}$$

$$2.33Ce_2O_{3(s,298K)} + 3SiO_{2(quartz,298K)} \rightarrow Ce_{4.67}(SiO_4)_3O_{(s,298K)} \tag{11}$$

In this way, we obtained $\Delta H_{f,ox}$ to be 421.4 ± 8.7 and −445.6 ± 11.6 kJ/mol (Table 5) from CeO_2 (eq 10), and from Ce_2O_3 (eq 11), respectively. Such a large difference between the two $\Delta H_{f,\ ox}$ values is because CeO_2 is more stable than Ce_2O_3 under the standard condition at RT. The ΔH_f for $Ce_{4.67}(SiO_4)_3O$ was then determined to be −7391.3 ± 9.5 kJ/mol or −7391.3 ± 14.7 kJ/mol. Furthermore, by combining the above results with enthalpies of formation of other isostructural rare-earth oxyapatites (Sm, Nd, Gd),[23] we established a linear variation of $\Delta H_{f,\ ox}$ against ionic potential (Figure 10): $\Delta H_{f,\ ox}$ (kJ/mol) = (−3374.4 ± 102.6) + (1106.3 ± 38.2) × Z/r) with an adjusted $R^2 = 0.996$. However, $La_{4.67}(SiO_4)_3O$ was found to be an outlier, as it significantly deviated from such a trend. Risbud et al.[23] argued that it could be due to the nonlinear effect of the ionic potential contributing to enthalpy.[23] However, with the newly available

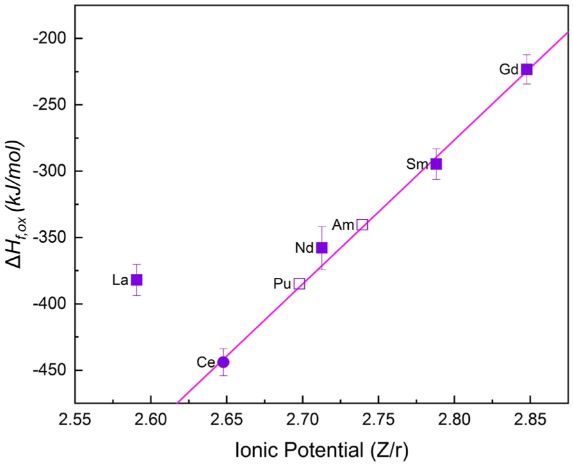

Figure 10. Variation of the enthalpies of formation of $RE_{4.67}(SiO_4)_3O$ from the oxides ($\Delta H_{f,\,ox}$) versus the ionic potential of Ln^{3+} cation ion. The equation describing the line is $\Delta H_{f,ox}$ (kJ/mol) = (−3374.4 ± 102.6) + (1106.3 ± 38.2) × (Z/r) with an adjusted $R^2 = 0.996$. Data reported for La, Nd, Sm, and Gd were extracted from Risbud et al. (2001)[23] while data associated with Pu and Am were evaluated from the fitted equation of the line and the known ionic radii in the 7-fold and 9-fold coordination environments.[68,117]

enthalpy of formation of $Ce_{4.67}(SiO_4)_3O$ we extended the linearity to beyond Nd, in which ionic radius range includes some important actinides, such as Am and Pu.

4. DISCUSSION

4.1. Aeronautic Applications of A-$Ce_2Si_2O_7$ or $Ce_{4.67}(SiO_4)_3O$.

As was stated earlier, one of the main expressed interest in rare earth silicate materials is their potentials as TBC or EBC against high-temperature degradation commonly encountered in aeronautical applications.[1,2,10−13] Desirable TBC and EBC materials must have both structural and chemical stabilities.[2,4,10−12,71−73] The structural stability includes congruent CTEs as the material that they are coating and phase stability at the operating temperature, which can minimize potential strains that promote mechanical failure.[1,2,4−9,73−75] The chemical inertness allows for inhibition of corrosion to the given material that they are coating. As many next-generation high-temperature alloys and CMC for aeronautical application offer superior thermal and mechanical properties at elevated temperature,[71,76] they often rapidly degrade in the presence of high-temperature air, steam, or mineral debris.[10−12,71] For this reason, the EBC or TBC must be chemically stable and resist against corrosion, to sustain the operating lifespan. Hence, to fully assess the suitability of the materials for aeronautical applications, we evaluated the high-temperature stability of both A-$Ce_2Si_2O_7$ and $Ce_{4.67}(SiO_4)_3O$ in terms of both structural and chemical stability.

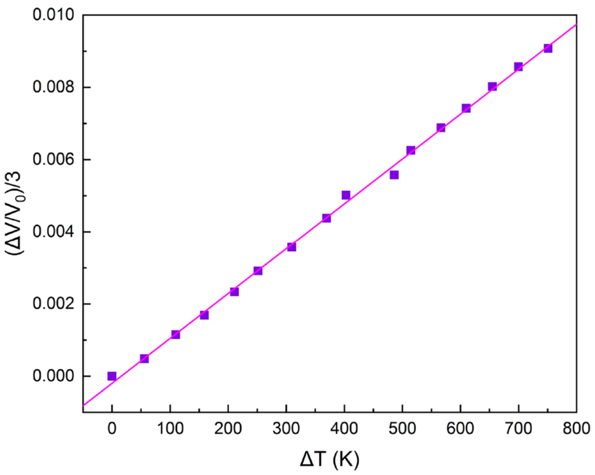

Figure 11. Variation of $(\Delta V/V_0)/3$ values versus ΔT obtained for the A-$Ce_2Si_2O_7$. The equation of the line describing the linear fitting is $(\Delta V/V_0)/3 = (-1.9604 \pm 0.5800) \times 10^{-4} + (1.2425 \pm 0.0130) \times 10^{-5} \times \Delta T$ with an adjusted $R^2 = 0.998$.

To assess the high-temperature structural stability of A-$Ce_2Si_2O_7$, we calculated the apparent bulk coefficients of thermal expansion (ABCTE)[1,7] so that a direct comparison to the data reported by Fernández-Carrión et al.[1] and Ayyasamy et al.[22] could be made. Here $(\Delta V/V_0)/3$ was plotted as a function of ΔT (Figure 11), where $\Delta V = V - V_0$ (V is the measured volume at each temperature and V_0 is the volume obtained at T_0) and ΔT is the temperature interval of collecting the HT-XRD data ($\Delta T = T - T_0$ and T_0 = 301 K). A linear relation was found, $(\Delta V/V_0)/3 = (-1.9604 \pm 0.5800) \times 10^{-4} + (1.2425 \pm 0.0130) \times 10^{-5} \times \Delta T$ (adjusted $R^2 = 0.998$), from which the ABCTE of A-$Ce_2Si_2O_7$ was evaluated to be 12.42×10^{-6} K^{-1} (Table 6).

Table 6. Apparent Bulk Coefficients of Thermal Expansion (ABCTE) Values for A-$RE_2Si_2O_7$ Compound and Their Average Ionic Radii of Each of the RE^{3+}[a]

chemical formula	avg. ionic radii of A-Site (Å)[68]	ABCTE (10^{-6} K^{-1})	reference
A-$Pr_2Si_2O_7$	1.137	11.8	Fernandez-Carrion et al. (2013)[1]
A-$Nd_2Si_2O_7$	1.121	10.5	Fernandez-Carrion et al. (2013)[1]
A-$La_2Si_2O_7$	1.173	14.0	Fernandez-Carrion et al. (2013)[1]
A-$Ce_2Si_2O_7$[b]	1.151	11.7	Ayyasamy et al. (2020)[22]
A-$Ce_2Si_2O_7$	1.151	12.4	this study

[a]The A-$RE_2Si_2O_7$ unit cell belongs to the $P4_1$ space group which exhibits four different crystallographic sites for the RE^{3+}. These four sites differ in coordination with having coordination numbers of 7, 8, 9, and 9. For this reason, averaging was done through taking the reported ionic size[68] of the RE^{3+} cation in each of the four coordination environments. [b]Calculated value

By combining the ABCTE value that we obtained in this paper for A-$Ce_2Si_2O_7$ with the already reported ABCTEs of other A-$Ln_2Si_2O_7$ (Ln = La, Nd, Pr),[1] one may generate a general trend for predicting the ABCTEs of unknown disilicate compounds within the $P4_1$ space group. It has been previously recognized that isostructural inorganic materials show an empirical correlation between thermodynamic variables, such as enthalpy,[64,77−81] free energy,[82,83] entropy,[84] or bulk modulus,[85,86] to underlying structural components, such as the cationic radii of a cation or the unit cell volume. So in this work, we used linear regression to determine the contributions of ionic radii to ABCTEs (Table 6)[1] with the predicted trend exhibited in Figure 12. Additionally, the ABCTE of A-$Ce_2Si_2O_7$ derived by machine learning reported in Ayyasamy et al.[22] agrees reasonably well (6% difference) with our value (12.42×10^{-6} K^{-1}) within the standard deviation of their predicted value. Such a smaller calculated ABCTE could be due to the underestimation of the unit cell volume of A-$Ce_2Si_2O_7$ (Table

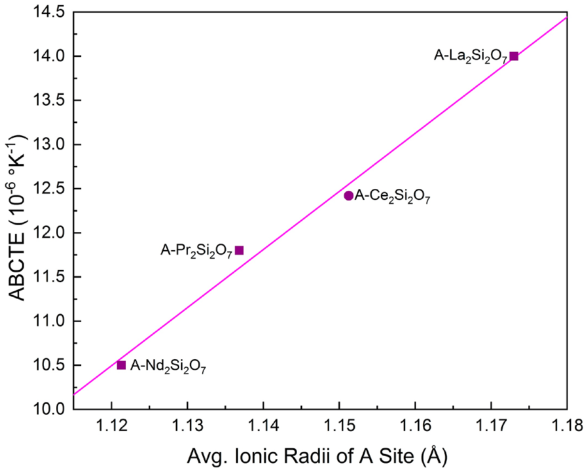

Figure 12. Comparison of ABCTE values of isostructural A-$RE_2Si_2O_7$ versus the average ionic size of the A site metal cation. Values shown as squares were extracted from Fernández-Carrión et al.,[1] while the value shown as a circle is from this study. The equation of the line describing the linear trend is ABCTE (10^{-6} K^{-1}) = (−63.2 ± 5.3) + (65.8 ± 4.7) × r, with an adjusted $R^2 = 0.985$. The A-$RE_2Si_2O_7$ unit cell belongs to the $P4_1$ space group which exhibits four different crystallographic sites for the RE^{3+}. These four sites differ in coordination with having coordination numbers of 7, 8, 9, and 9. For this reason, averaging was done through taking the reported ionic size[68] of the RE^{3+} cation in the four coordination environments, values reported in Table 6.

7).[22] With such a high CTE, there could be applications for A-$Ce_2Si_2O_7$ for utilization as TBC of a metal substrate.[1] However, when considering high-temperature structural stability, the A-$Ce_2Si_2O_7$ → G-$Ce_2Si_2O_7$ transition at 1547 K could be considered as a drawback. As the temperature of the rear outlet in next-generation combustion engines will need to exceed 2123 K,[2] such a transition is probable to occur. This will cause a large reduction in the unit cell volume (~46%)[14] and a decrease in the CTE by roughly half (Table 1).[1] Such a reduction in both unit cell volume and CTE may cause a mechanical strain on the system, resulting in cracks and fissures to develop.

The assessment of the chemical stability of A-$Ce_2Si_2O_7$ was based on four reactions occurring in the presence of oxygen or water at 1300 K

$$Ce_2Si_2O_{7(s,1300K)} + 0.5O_{2(g,1300K)} \rightarrow 2CeSiO_{4(s,1300K)} \quad (12)$$

$$Ce_2Si_2O_{7(s,1300K)} + 0.5O_{2(g,1300K)} \rightarrow 2CeO_{2(s,1300K)} + 2SiO_{2(cristobalite,1300K)} \quad (13)$$

$$Ce_2Si_2O_{7(s,1300K)} + H_2O_{(g,1300K)} \rightarrow 2CeSiO_{4(s,1300K)} + H_{2(g,1300K)} \quad (14)$$

$$Ce_2Si_2O_{7(s,1300K)} + H_2O_{(g,1300K)} \rightarrow 2CeO_{2(s,1300K)} + 2SiO_{2(cristobalite,1300K)} + H_{2(g,1300K)} \quad (15)$$

The temperature of 1300 K was chosen because it is below the A-$Ce_2Si_2O_7$ → G-$Ce_2Si_2O_7$ transition. The thermodynamic stability of any given reaction is dictated by the Gibbs free energy $\Delta G = \Delta H - TS$, which requires both enthalpy and entropy. To date, there has been no experimentally reported $S°(298\ K)$ value of either A-$Ce_2Si_2O_7$ or $CeSiO_4$. However, the $S°$ value can be estimated through an empirical relation between the formula unit volume ($V_m = V_{cell}$/formula units (Z))[87] and the standard entropies for silicate minerals.[84] We verified the accuracy of such method by calculating $S°(298\ K)$ of zircon, with the difference between the benchmarked (84.0 ± 1.3 J/(mol·K))[88] and the estimated (85.1 ± 2.6 J/(mol·K)) being only 1.3%. The molar volumes V_m of A-$Ce_2Si_2O_7$ and of $CeSiO_4$ are 1143.40(2) Å^3/8 (Table 2) and 298.93(1) Å^3/4,[89] respectively. The corresponding $S°(298\ K)$ were estimated to be 186.2 ± 5.6 J/(mol·K) and 97.9 ± 2.9 J/(mol·K), respectively. By combining with $S°(298\ K)$ of the constituent elements,[88] $S°_f$ was calculated and subsequently applied to evaluate $\Delta G°_f$ and ΔG_{rxn} (Table S2). The above methodology has been used successfully in estimating $\Delta G°_f$ of polyhalite ($K_2Ca_2Mg(SO_4)_4 \cdot 2H_2O$) to determine its stability in a mined geological repository.[90] In order to obtain ΔH_f(1300K), we used the thermodynamic function

$$\Delta H(T) = \Delta H(298K) + \int_{298K}^{T} \Delta C_p \, dT \quad (16)$$

When the C_p data of a given phase was not available, the Neumann-Kopp's rule was used. Neumann-Kopp's rule states that C_p of a complex oxide can be calculated through the summation of known C_p of its constituent binary oxides.[91] We also verified such approximation by comparing the estimated C_p value with those reported for $ZrSiO_4$[88] and G-$Ce_2Si_2O_7$.[92] For zircon, the difference between the two C_p values differed by a maximum of 1.1% over the temperature range of 500−1400 K. This was deemed acceptable to use for obtaining a C_p value for $CeSiO_4$. Conversely, for G-$Ce_2Si_2O_7$, it was found that the estimation underestimated the benchmarked C_p value by 6.1% at 1000 K (Figure S3). For this reason, we have chosen to use the experimentally derived C_p value of G-$Ce_2Si_2O_7$[92] for A-$Ce_2Si_2O_7$ instead of using the C_p obtained through the Neumann-Kopp estimation. Here, we extended the benchmarked C_p equation of G-$Ce_2Si_2O_7$ from 900 K[92] to 1300 K using a fifth-order polynomial fit (Figure S3). The equation describing the new C_p data is $y = (-29.42 \pm 1.141) +$

Table 7. Reported Unit Cell Parameters for A-$Ce_2Si_2O_7$

chemical	a (Å)	c (Å)	volume (Å^3)	reference
A-$Ce_2Si_2O_7$	6.7964(3)	24.7282(14)	1142.22(10)	Deng and Ibers (2005)[58]
A-$Ce_2Si_2O_7$	6.7920	24.7000	1139.38	Tas and Akinc (1994)[27]
percleveite-(Ce)	6.7805(8)	24.689(5)	1135.1(3)	Holtstam et al. (2003)[34]
A-$Ce_2Si_2O_7$	6.75781	24.5511	1121.20	Ayyasamy et al. (2020)[22]
A-$Ce_2Si_2O_7$	6.7965(3)	24.7258(14)	1142.1(1)	Estevenon et al. (2019)[37]
A-$Ce_2Si_2O_7$	6.79901(7)	24.7346(2)	1143.40(2)	this study

$(1.518 \pm 0.025) \times x + (-0.004 \pm 0.025) \times x^2 + (4.533 \pm 0.432) \times 10^{-6} \times x^3 + (-2.881 \pm 0.491) \times 10^{-9} \times x^4 + (7.260 \pm 1.993) \times 10^{-13} \times x^5$ with an adjusted R^2 of 0.999 (Table S2).

When evaluating the calculated ΔG_{rxn} of reactions (Table S2), it is clear that A-$Ce_2Si_2O_7$ is chemically unstable in the presence of oxygen or steam at 1300 K and should undergo exothermic decomposition reactions into CeO_2 and SiO_2. This was demonstrated through $\Delta G_{\mathrm{rxn}}(13) = -182.7 \pm 10.7$ kJ/mol and $\Delta G_{\mathrm{rxn}}(14) = -223.3 \pm 10.7$ kJ/mol. The high-temperature decomposition of A-$Ce_2Si_2O_7$ into $CeSiO_4$ in the presence of air at 1300 K (reaction 12) was found to be favorable because of the negative value of ΔH_{rxn}(1300 K), −188.1 kJ/mol. This reaction was found to be −39.4 kJ/mol more favorable to occur than the degradation of A-$Ce_2Si_2O_7$ into CeO_2 and SiO_2 (ΔH_{rxn}(1300 K) = −148.7 kJ/mol). Nevertheless, due to the increased importance of the S term in assessing the thermodynamic stability (ΔG) at elevated temperatures, the reaction was ultimately found to be thermodynamically unfavorable, with $\Delta G_{\mathrm{rxn}}(12) = 66.7 \pm 13.2$ kJ/mol at 1300 K (Table S2).

An overall evaluation of the suitability of $Ce_{4.67}(SiO_4)_3O$ for high-temperature aeronautical applications can be made by analyzing the results of *in situ* HT-XRD (Figure 5) and TGA-DSC (Figure 9), both of which showed a thermal decomposition into a mixture of its binary oxides in the presences of O_2 at elevated temperatures. Therefore, from both a structural and chemical stability standpoint $Ce_{4.67}(SiO_4)_3O$ is not a good EBC or TBC material for high-temperature applications. However, it is known that various rare-earth oxyapatites ($M^{2+}RE_4(SiO_4)_3O$) form as corrosion products between the rare-earth disilicates EBC and molten aerosol CMAS mineral dust,[10,11,93] which implies that the cation-vacancy rare-earth oxyapatite ($RE_{4.67}(SiO_4)_3O$) may also form under such conditions. More generally, $RE_{4.67}(SiO_4)_3O$ exhibits less negative enthalpy of formation values compared to $Ca^{2+}RE_4(SiO_4)_3O$ determined by Costa et al.[11] However, the higher disordering in the cation-vacancy phase has greater entropic contribution at high temperatures which could lead to its formation in the presence of molten CMAS. However, at temperature above ∼1000 K $Ce_{4.67}(SiO_4)_3O$ is not thermally stable in the presence of O_2 and will decompose into CeO_2 and SiO_2.

4.2. Understanding of the Mineral Formation of Stetindite and Percleveite.

With the enthalpies of formation available now for the two naturally occurring cerium silicate phases of stetindite ($CeSiO_4$) and percleveite (A-$Ce_2Si_2O_7$), we can evaluate their formation under relevant geological settings, aiming to shed new light of the overall rarity. $\Delta H_{\mathrm{f,ox}}$ of stetindite was reported to be 27.5 ± 3.1 kJ/mol.[33] This moderately endothermic $\Delta H_{\mathrm{f,ox}}$ explains the difficulty in synthesizing $CeSiO_4$ in the laboratory and its rarity in nature because it is metastable with respect to its two binary oxides (CeO_2 and SiO_2), as it is found for coffinite.[33,61,94−96] $\Delta H_{\mathrm{f,ox}}$ of percleveite from CeO_2 and SiO_2 is 173.7 ± 5.5 kJ/mol, which also indicates that the formation of percleveite is not favorable.

Despite being thermodynamically unstable, both stetindite and percleveite have been found in mineral deposits. The geologic setting where these two minerals have been identified does differ from one another. Stetindite was discovered at the Stetind pegmatite of the Tysfjord granite located in Norway.[36] Percleveite was discovered in an old museum specimen originating from the Bastnäs hydrothermal deposit located in Sweden and has since only been found within this specimen.[34] A possible explanation is that the mineral formation is largely dictated by the local redox conditions in the deposit. Mineral redox buffer assemblages are often used in the geochemical system to fix the oxygen fugacity (f_{O_2}).[97] Common mineral redox buffer assemblages include quartz−fayalite−magnetite (QFM), nickel−nickel oxide (Ni/NiO), and hematite−magnetite (Fe_2O_3/Fe_3O_4).[97] Particularly, hematite was found to be associated with the mineral deposit where stetindite was discovered,[36] creating a localized oxidizing environment, allowing for Ce^{4+} to form through the oxidation of Ce^{3+}-fluoride complex or other Ce^{3+} silicates such as percleveite.[36,98] This does bear a similarity to the procedure described by Estevenon et al. for the hydrothermal synthesis of $CeSiO_4$ from both aqueous and solid precursors.[37,99] Furthermore, the enthalpy of reaction of A-$Ce_2Si_2O_7$ → $CeSiO_4$ at room temperature was evaluated to be -59.4 ± 4.1 kJ/mol per mole of Ce (and -63.8 ± 3.6 kJ/mol per mole of Ce for $Ce_{4.67}(SiO_4)_3O$ → $CeSiO_4$), and the Gibbs free energy of reaction under 523 K (the synthesis temperature for $CeSiO_4$)[37] to be -22.6 ± 7.9 per mole of Ce (and -5.7 ± 7.2 kJ/mol per mole of Ce for $Ce_{4.67}(SiO_4)_3O$ → $CeSiO_4$), suggesting a favorable chemical formation of tetravalent cerium orthosilicate from trivalent cerium silicates. Thus, under geologic conditions Ce^{3+} silicates could serve as potential solid precursors if the local redox of the deposit conditions became oxidizing, such as what was observed at the deposit where stetindite was discovered.[36,98] For percleveite, magnetite is associated with the mineral deposit,[34] acting as the redox buffer controlling the formation of percleveite. It is further supported by the thermodynamically favorable enthalpy of formation of percleveite from Ce_2O_3 and SiO_2, -197.9 ± 7.4 kJ/mol. This is also consistent with the synthetic procedure of A-$Ce_2Si_2O_7$ where a high-temperature reducing condition (H_2 atmosphere) was used to suppress the oxidative formation of CeO_2.[14,16,21,27,37]

While the above offers both a formational mechanism for $CeSiO_4$ in nature and its overall rarity, it does not offer a direct explanation to why A-$Ce_2Si_2O_7$ is so rare in nature. As the mineral assemblages to form a reducing environment are possible to occur across the entire spectrum of the igneous classification, from mafic to felsic,[44,97] and as Ce concentrations are also relatively conserved across the igneous classification,[100,101] one would expect percleveite to be observed at more than one mineral deposit.[34,102] Interestingly, through mineral texture analysis it has been determined that percleveite formed as a primary mineral during the early stages of the hydrothermal history of the Bastnäs deposit.[34] In addition, the more widely abundant minerals of allanite ($(Ca,Ce)_2(AlFe^{3+})_3(Si_2O_7)(SiO_4)O(OH)$) and bastnäsite ($REECO_3F$) have been determined to be secondary minerals, forming later in the hydrothermal history of the Bastnäs deposit, and reflect an overall change in the chemistry of the hydrothermal fluid.[34,103] With such a chronology being further supported by the discovery of bastnäsite-(Ce) growing at the expense of the percleveite holotype.[102] Subsequently, this observed parasitic mineral formation can explain the rarity of percleveite as it serves as a precursor for the more commonly observed hydrothermal REE minerals (i.e., allanite or bastnäsite). This hypothesis is similar to the proposed explanation for the rarity of fluocerite ($REEF_3$), which also forms as a primary mineral and is later converted to bastnäsite in the presence of carbonate-rich fluids.[102,104,105]

4.3. Relevance in the Field of the Nuclear Fuel Cycle.

Although $Ce_{4.67}(SiO_4)_3O$ and other cation vacant rare earth oxyapatite have not been discovered as natural phases, they do find significant relevance to both the middle and end of the "cradle to grave" aspect of the nuclear fuels cycle. For example, when simulating the vitrification process for immobilizing nuclear waste in alumino-borosilicate glasses it was found that Dy and Ho cation-vacant oxyapatites formed within the simulated nuclear waste glass.[106] Further, in a study using cerium silicide (a surrogate for uranium silicide fuel) to evaluate the performance under the hydrothermal conditions (573 K and 9 MPa) presented in a light water reactor (LWR), $Ce_{4.67}(SiO_4)_3O$ was always found as a corrosion layer to cerium silicide.[107] Therefore, it is clear that $An_{4.67}(SiO_4)_3O$ type-materials could be also potentially formed during the long-term storage under geological repository resulting in the breach of the radiological waste canister. Assuming the former scenario, the enthalpies of formation of $Am_{4.67}(SiO_4)_3O$ and $Pu_{4.67}(SiO_4)_3O$ from oxides were predicted to be −340.4 and −384.9 kJ/mol, respectively, based on the linear relation given in Figure 10. A similar methodology was utilized for predicting $\Delta H_{f,\,ox}$ for actinide orthosilicates.[33]

In the mined geological repository, the local redox environment would be fixed to be reducing.[108−110] Achieving such reducing environments can be done through controlling the fugacity of oxygen and other gases through various mineral assemblages, as was described in the previous section.[97] Such engineering was demonstrated at the Waste Isolation Pilot Plant (WIPP) in New Mexico, U.S.A., where periclase (MgO) was used to hinder the microbial breakdown of organics and scavenge for CO_2.[111] The presence of the remaining organics could further lead to reducing conditions in the repository. Thus, it is reasonable to assume that in the unlikely event of canister failure, the waste package will interact with infiltrated groundwater under a reducing environment. Under such conditions, Pu could be found in the trivalent state and readily involved in the formation of $Pu_{4.67}(SiO_4)_3O$. For Am, these findings are slightly more significant due to its predominant trivalent oxidation state.[112−115] Therefore, if any Am^{3+} would react with silica it would be thermodynamically favorable to form $Am_{4.67}(SiO_4)_3O$. However, if the redox environment becomes strongly oxidative, a transformation from trivalent actinide silicates to the tetravalent actinide orthosilicate may occur driven by thermodynamics, such as that demonstrated in the case of A-$Ce_2Si_2O_7$ → $CeSiO_4$ or $Ce_{4.67}(SiO_4)_3O$ → $CeSiO_4$. Finally, as actinides are known to form nanoparticles in reactive silicate rich fluids,[45−48] it could enable the actinide silicate complexes or compounds to be transported in colloidal forms immense distances away from a breached canister if the particles would not settle.[53,54]

5. CONCLUSIONS

Through thermogravimetric analysis coupled with differential scanning calorimetry (TGA-DSC), *in situ* high temperature synchrotron XRD, and high temperature oxide melt drop solution calorimetry, the thermodynamic parameters of percleveite (A-$Ce_2Si_2O_7$) and cerium oxyapatite ($Ce_{4.67}(SiO_4)_3O$) were determined. The results of the TGA-DSC confirmed that percleveite and cerium oxyapatite were thermally stable under nitrogen. However, both the TGA-DSC and *in situ* synchrotron HT-XRD showed that cerium oxyapatite was not thermally stable under an oxygen atmosphere undergoing a slow partial oxidation of Ce^{3+} to new nonstoichiometric phases $Ce^{3+}{}_{1.67-x}Ce^{4+}{}_xCe^{3+}{}_3(SiO_4)_3O_{1+0.5x}$, which then decomposed to CeO_2 and SiO_2 above ~1000 K. *In situ* synchrotron HT-XRD revealed that the ABCTE of percleveite is 12.4×10^{-6} K^{-1}, which follows the systematic linear trend exhibited by the other A-$RE_2Si_2O_7$ ($P4_1$). Through high temperature oxide melt drop solution calorimetry, the ΔH_f was determined to be −3825.1 ± 6.0 kJ/mol for percleveite and −7391.3 ± 9.5 kJ/mol for cerium oxyapatite. We further evaluated the roles of A-$Ce_2Si_2O_7$ and $Ce_{4.67}(SiO_4)_3O$ as TBC/EBC or potential degradation products in the field of high-temperature applications, and as possible alteration phases and surrogate materials in the geological nuclear waste repository. Lastly, the geological relevance of percleveite was discussed as well as its overall role as a possible precursor for allanite-(Ce) and stetindite.

■ ASSOCIATED CONTENT

Supporting Information

The Supporting Information is available free of charge at https://pubs.acs.org/doi/10.1021/acsearthspacechem.0c00231.

PXRD, thermodynamic data, and thermochemical tables (PDF)

■ AUTHOR INFORMATION

Corresponding Author

Xiaofeng Guo − *Department of Chemistry, Alexandra Navrotsky Institute for Experimental Thermodynamics, and Materials Science and Engineering, Washington State University, Pullman, Washington 99164, United States;* orcid.org/0000-0003-3129-493X; Email: x.guo@wsu.edu

Authors

Andrew C. Strzelecki − *Department of Chemistry, Alexandra Navrotsky Institute for Experimental Thermodynamics, and Materials Science and Engineering, Washington State University, Pullman, Washington 99164, United States*

Kyle Kriegsman − *Department of Chemistry and Alexandra Navrotsky Institute for Experimental Thermodynamics, Washington State University, Pullman, Washington 99164, United States*

Paul Estevenon − *ICSM, Univ Montpellier, CNRS, CEA, ENSCM, Bagnols sur Cèze 30207, France; CEA, DES, ISEC, DMRC, Univ Montpellier, Site de Marcoule 30207, France*

Vitaliy Goncharov − *Department of Chemistry, Alexandra Navrotsky Institute for Experimental Thermodynamics, and Materials Science and Engineering, Washington State University, Pullman, Washington 99164, United States*

Jianming Bai − *National Synchrotron Light Source II, Brookhaven National Laboratory, Upton, New York 11973, United States;* orcid.org/0000-0002-0575-2987

Stephanie Szenknect − *ICSM, Univ Montpellier, CNRS, CEA, ENSCM, Bagnols sur Cèze 30207, France;* orcid.org/0000-0003-3691-3621

Adel Mesbah − *ICSM, Univ Montpellier, CNRS, CEA, ENSCM, Bagnols sur Cèze 30207, France;* orcid.org/0000-0002-6905-2402

Di Wu − *Department of Chemistry, Alexandra Navrotsky Institute for Experimental Thermodynamics, Materials Science and Engineering, and The Gene and Linda Voiland School of*

Chemical Engineering and Bioengineering, Washington State University, Pullman, Washington 99164, United States; orcid.org/0000-0001-6879-321X

John S. McCloy − *Department of Chemistry, Materials Science and Engineering, and School of Mechanical and Materials Engineering, Washington State University, Pullman, Washington 99164, United States;* orcid.org/0000-0001-7476-7771

Nicolas Dacheux − *ICSM, Univ Montpellier, CNRS, CEA, ENSCM, Bagnols sur Cèze 30207, France;* orcid.org/0000-0003-1636-1313

Complete contact information is available at: https://pubs.acs.org/10.1021/acsearthspacechem.0c00231

Author Contributions

X.G. conceived the research. A.C.S. and K.W.K. performed DSC and high-temperature drop solution oxide melt calorimetry. P.E. synthesized all phases. X.G., V.G.G., and J.B. performed ambient and high-temperature synchrotron XRD. A.C.S and X.G. analyzed and refined all the ambient and high-temperature synchrotron XRD. All authors participated in discussions, interpretation of the data, and writing of the manuscript.

Notes

The authors declare no competing financial interest.

■ ACKNOWLEDGMENTS

This work was supported by the institutional funds from the Department of Chemistry at Washington State University. We also acknowledge the support by the U.S. Department of Energy, Office of Nuclear Energy, Grants DE-NE0008582 and DE-NE0008689. This research used Beamline 28-ID-2 (XPD) of the National Synchrotron Light Source II, a U.S. Department of Energy (DOE) Office of Science User Facility operated for the DOE Office of Science by Brookhaven National Laboratory under Contract No. DE-SC0012704. Portions of this research were also supported by collaboration, services, and infrastructure through the Nuclear Science Center User Facility at WSU, the WSU-PNNL Nuclear Science and Technology Institute, and Alexandra Navrotsky Institute for Experimental Thermodynamics. We are grateful for the discussions and comments with A.A. Migdissov, in particular for his guidance in understanding mineral redox buffers. Lastly, we thank A. Navrotsky for supplying us Pt crucibles and lead borate solvent for the calorimetric experiments in this work.

■ REFERENCES

(1) Fernández-Carrión, A. J.; Allix, M.; Becerro, A. I. Thermal Expansion of Rare-Earth Pyrosilicates. *J. Am. Ceram. Soc.* **2013**, *96* (7), 2298−2305.

(2) Xu, Y.; Hu, X.; Xu, F.; Li, K. Rare Earth Silicate Environmental Barrier Coatings: Present Status and Prospective. *Ceram. Int.* **2017**, *43* (8), 5847−5855.

(3) Zhu, D. Aerospace Ceramic Materials: Thermal, Environmental Barrier Coatings and SiC/SiC Ceramic Matrix Composites for Turbine Engine Applications. *NASA TM-2018-219884*; National Aeronautical Space Administration (NASA), Glenn Research Center, 2018, pp 1−30.

(4) Lee, K. N.; Fox, D. S.; Bansal, N. P. Rare Earth Silicate Environmental Barrier Coatings for SiC/SiC Composites and Si_3N_4 Ceramics. *J. Eur. Ceram. Soc.* **2005**, *25* (10), 1705−1715.

(5) Wang, Y. Q.; Huang, J. F.; Cao, L. Y.; Zeng, X. R. $Y_2Si_2O_7$ Whisker Reinforced $MoSi_2$ Multi-Composition Coating for SiC Pre-Coated Carbon/Carbon Composites. *Adv. Compos. Mater.* **2011**, *20* (2), 125−132.

(6) Cao, X. Q.; Vassen, R.; Stoever, D. Ceramic Materials for Thermal Barrier Coatings. *J. Eur. Ceram. Soc.* **2004**, *24* (1), 1−10.

(7) Dolan, M. D.; Harlan, B.; White, J. S.; Hall, M.; Misture, S. T.; Bancheri, S. C.; Bewlay, B. Structures and Anisotropic Thermal Expansion of the α, β, γ, and δ Polymorphs of $Y_2Si_2O_7$. *Powder Diffr.* **2008**, *23* (1), 20−25.

(8) Fukuda, K.; Matsubara, H. Thermal Expansion of Delta-Yttrium Disilicate Koichiro. *J. Am. Ceram. Soc.* **2004**, *87*, 89−92.

(9) Aparicio, M.; Durán, A. Yttrium Silicate Coatings for Oxidation Protection of Carbon- Silicon Carbide Composites. *J. Am. Ceram. Soc.* **2000**, *83* (6), 1351−1355.

(10) Costa, G.; Harder, B. J.; Wiesner, V. L.; Jacobson, N. S.; Zhu, D.; Kapush, D.; Bansal, N.; Lee, K. N.; Ushakov, S. V.; Navrotsky, A. Thermodynamics of Reaction between Gas - Turbine Ceramic Coatings and Ingested CMAS Corrodents. *J. Am. Ceram. Soc.* **2018**, 2948−2964.

(11) Costa, G.; Harder, B. J.; Bansal, N. P.; Kowalski, B. A.; Stokes, J. L. Thermochemistry of Calcium Rare-Earth Silicate Oxyapatites. *J. Am. Ceram. Soc.* **2020**, *103* (2), 1446−1453.

(12) Webster, R. I.; Bansal, N. P.; Salem, J. A.; Opila, E. J.; Wiesner, V. L. Characterization of Thermochemical and Thermomechanical Properties of Eyjafjallajökull Volanic Ash Glass. *Coatings* **2020**, *10* (2), 100.

(13) Poerschke, D. L.; Jackson, R. W.; Levi, C. G. Silicate Deposit Degradation of Engineered Coatings in Gas Turbines: Progress Toward Models and Materials Solutions. *Annu. Rev. Mater. Res.* **2017**, *47* (1), 297−330.

(14) Felsche, J. Polymorphism and Crystal Data of the Rare-Earth Disilicates of Type $R.E._2Si_2O_7$. *J. Less-Common Met.* **1970**, *21*, 1−14.

(15) Felsche, J. Rare Earth Silicates with the Apatite Structure. *J. Solid State Chem.* **1972**, *5* (2), 266−275.

(16) Felsche, J.; Hirsiger, W. The Polymorphs of the Rare-Earth Pyrosilicates $R.E._2Si_2O_7$, [R.E.: La, Ce, Pr, Nd, Sm]. *J. Less-Common Met.* **1969**, *18* (2), 131−137.

(17) Zec, S.; Boskovic, S. Cerium Silicates Formation from Mechanically Activated Oxide Mixtures. *J. Mater. Sci.* **2004**, *39* (16−17), 5283−5286.

(18) Kepiński, L.; Wołcyrz, M.; Marchewka, M. Structure Evolution of Nanocrystalline CeO_2 Supported on Silica: Effect of Temperature and Atmosphere. *J. Solid State Chem.* **2002**, *168* (1), 110−118.

(19) Kępiński, L.; Hreniak, D.; Stręk, W. Microstructure and Luminescence Properties of Nanocrystalline Cerium Silicates. *J. Alloys Compd.* **2002**, *341* (1−2), 203−207.

(20) Ghannadi Marageh, M.; Waqif Husain, S.; Khanchi, A.R.; Ahmady, S.J. Sorption Studies of Radionuclides on a New Ion Exchanger: Cerium (III) Silicate. *Appl. Radiat. Isot.* **1996**, *47* (5−6), 501−505.

(21) Felsche, J. The Crystal Chemistry of the Rare-Earth Silicates. In *Structure and Bonding: Rare Earths*; Springer Berlin Heidelberg: Berlin, 1973; pp 99−197.

(22) Ayyasamy, M. V.; Deijkers, J. A.; Wadley, H. N. G.; Balachandran, P. V. Density Functional Theory and Machine Learning Guided Search for $RE_2Si_2O_7$ with Targeted Coefficient of Thermal Expansion. *J. Am. Ceram. Soc.* **2020**, *103*, 4489.

(23) Risbud, A. S.; Helean, K. B.; Wilding, M. C.; Lu, P.; Navrotsky, A. Enthalpies of Formation of Lanthanide Oxyapatite Phases. *J. Mater. Res.* **2001**, *16* (10), 2780−2783.

(24) Fukuda, K.; Asaka, T.; Uchida, T. Thermal Expansion of Lanthanum Silicate Oxyapatite ($La_{9.332x}(SiO_4)_6O_{23x}$), Lanthanum Oxyorthosilicate (La_2SiO_5) and Lanthanum Sorosilicate ($La_2Si_2O_7$). *J. Solid State Chem.* **2012**, *194*, 157−161.

(25) Cordfunke, E. H. P.; Booij, A. S.; Van Der Laan, R. R. The Thermochemical Properties of $Y_2Si_2O_7$ and $Dy_2Si_2O_7$. *J. Chem. Thermodyn.* **1998**, *30*, 199−205.

(26) Tas, A. C.; Akinc, M. Cerium Oxygen Apatite ($Ce_{4.67}[SiO_4]_3O$) X-Ray Diffraction Pattern Revisited. *Powder Diffr.* **1992**, *7* (4), 219−222.

(27) Tas, A. C.; Akinc, M. Phase Relations in the System Ce_2O_3−$Ce_2Si_2O_7$ in the Temperature Range 1150° to 1970°C in Reducing and Inert Atmospheres. *J. Am. Ceram. Soc.* **1994**, *77* (11), 2953−2960.

(28) Bünzli, J.-C. G.; McGill, I. *Rare Earth Elements*; Wiley-VCH Verlag GmbH & Co. KGaA, 2018.

(29) Zamoryanskaya, M. V.; Burakov, B. E. Feasibility Limits in Using Cerium as a Surrogate for Plutonium Incorporation in Zircon, Zirconia and Pyrochlore. *Mater. Res. Soc. Symp. - Proc.* **2000**, *663*, 301−306.

(30) Putnam, R. L.; Navrotsky, A.; Cordfunke, E. H. P.; Huntelaar, M. E. Thermodynamics of Formation of Two Cerium Aluminum Oxides, $CeAlO_{3(s)}$ and $CeAl_{12O19.918(s)}$, and Cerium Sesquioxide,- $Ce_2O_{3(s)}$ At T= 298.15 K. *J. Chem. Thermodyn.* **2000**, *32* (7), 911−921.

(31) Putnam, R. L.; Gallegos, U. F.; Ebbinghaus, B. B.; Navrotsky, A.; Helean, K. B.; Ushakov, S. V; Woodfield, B. F.; Boerio-Goates, J.; Williamson, M. A. Formation Energetics of Ceramic Phases Related to Surplus Plutonium Disposition. In *Environmental Issues and Waste Management Technologies VI, Ceramic Transactions*; Vol. *119*, The American Ceramic Society: Los Alamos, NM, 2001, pp 147−158.

(32) Marra, J. C.; Cozzi, A. D.; Pierce, R. A.; Pareizs, J. M.; Jurgensen, A. R.; Missimer, D. M. Cerium as a Surrogate in the Plutonium Immobilized Form. In Environmental Issues and Waste Management Technologies in the Ceramic and Nuclear Industries; Smith, G. L., Sundaram, S. K., Spearing, D. R., Eds.; *American Ceramic Society*, 2002; pp 381−388.

(33) Strzelecki, A. C.; Bourgeois, C.; Kriegsman, K. W.; Estevenon, P.; Wei, N.; Szenknect, S.; Mesbah, A.; Wu, D.; Ewing, R. C.; Dacheux, N.; Guo, X. Thermodynamics of $CeSiO_4$: Implications for Actinide Orthosilicates. *Inorg. Chem.* **2020**, *59* (18), 13174−13183.

(34) Holtstam, D.; Norrestam, R.; Andersson, U. B. Percleveite-(Ce)- A New Lanthanide Disilicate Mineral from Bastnäs, Skinnskatteberg, Sweden. *Eur. J. Mineral.* **2003**, *15* (4), 725−731.

(35) Li, Y.; Zhang, T.; Liu, C.; Jiang, M. Thermodynamic and Experimental Studies on Al Addition of 253MA Steel. *Metals (Basel, Switz.)* **2019**, *9* (4), 433.

(36) Schlüter, J.; Malcherek, T.; Husdal, T. A. The New Mineral Stetindite, $CeSiO_4$, a Cerium End-Member of the Zircon Group. *Neues Jahrb. Mineral., Abh.* **2009**, *186* (2), 195−200.

(37) Estevenon, P.; Kaczmarek, T.; Vadot, F.; Dumas, T.; Solari, P. L.; Welcomme, E.; Szenknect, S.; Mesbah, A.; Moisy, P.; Poinssot, C.; Dacheux, N. Formation of $CeSiO_4$ from Cerium (III) Silicate Precursors. *Dalt. Trans.* **2019**, *48*, 10455−10463.

(38) Estevenon, P.; Welcomme, E.; Tamain, C.; Jouan, G.; Szenknect, S.; Mesbah, A.; Poinssot, C.; Moisy, P.; Dacheux, N. Formation of $PuSiO_4$ under Hydrothermal Conditions. *Dalt. Trans.* **2020**, *49*, 6434.

(39) Buscheck, T. A.; Glascoe, L. G.; Lee, K. H.; Gansemer, J.; Sun, Y.; Mansoor, K. Validation of the Multiscale Thermohydrologic Model Used for Analysis of a Proposed Repository at Yucca Mountain. *J. Contam. Hydrol.* **2003**, *62*−*63*, 421−440.

(40) Haukwa, C. B.; Wu, Y. S.; Bodvarsson, G. S. Modeling Thermal-Hydrological Response of the Unsaturated Zone at Yucca Mountain, Nevada, to Thermal Load at a Potential Repository. *J. Contam. Hydrol.* **2003**, *62*−*63*, 529−552.

(41) Löfman, J. Simulation of Hydraulic Disturbances Caused by the Decay Heat of the Repository in Olkiluoto Simulation of Hydraulic Disturbances Caused by the Decay Heat of the Repository in Olkiluoto. *Technical Report POSIVA 2005-07*; POSIVA OY: Olkiluoto, Finland, 2005.

(42) Zhou, W.; Apted, M. J.; Kessler, J. H. The Thermal-Hydrological Impact on Increased Spent-Fuel Storage Capacity in Yucca Mountain Repository. *Nucl. Technol.* **2010**, *170* (2), 336−352.

(43) Blanco Martín, L.; Rutqvist, J.; Birkholzer, J. T. Long-Term Modeling of the Thermal-Hydraulic-Mechanical Response of a Generic Salt Repository for Heat-Generating Nuclear Waste. *Eng. Geol.* **2015**, *193*, 198−211.

(44) Winter, J. D. *Principles of Igneous and Metamorphic Petrology*, 2nd ed.; Pearson, 2013.

(45) Estevenon, P.; Causse, J.; Szenknect, S.; Welcomme, E.; Mesbah, A.; Moisy, P.; Poinssot, C.; Dacheux, N. In-Situ Study of the Synthesis of Thorite ($ThSiO_4$) under Environmental Representative Conditions. *Dalt. Trans.* **2020**, *49*, 11512.

(46) Neill, T. S.; Morris, K.; Pearce, C. I.; Sherriff, N. K.; Burke, M. G.; Chater, P. A.; Janssen, A.; Natrajan, L.; Shaw, S. Stability, Composition, and Core-Shell Particle Structure of Uranium(IV)-Silicate Colloids. *Environ. Sci. Technol.* **2018**, *52* (16), 9118−9127.

(47) Hennig, C.; Weiss, S.; Banerjee, D.; Brendler, E.; Honkimäki, V.; Cuello, G.; Ikeda-Ohno, A.; Scheinost, A. C.; Zänker, H. Solid-State Properties and Colloidal Stability of Thorium(IV)-Silica Nanoparticles. *Geochim. Cosmochim. Acta* **2013**, *103*, 197−212.

(48) Zänker, H.; Weiss, S.; Hennig, C.; Brendler, V.; Ikeda-Ohno, A. Oxyhydroxy Silicate Colloids: A New Type of Waterborne Actinide-(IV) Colloids. *ChemistryOpen* **2016**, *5* (3), 174−182.

(49) Estevenon, P.; Welcomme, E.; Szenknect, S.; Mesbah, A.; Moisy, P.; Poinssot, C.; Dacheux, N. Multiparametric Study of the Synthesis of $ThSiO_4$ under Hydrothermal Conditions. *Inorg. Chem.* **2018**, *57* (15), 9393−9402.

(50) Szenknect, S.; Mesbah, A.; Cordara, T.; Clavier, N.; Brau, H. P.; Le Goff, X.; Poinssot, C.; Ewing, R. C.; Dacheux, N. First Experimental Determination of the Solubility Constant of Coffinite. *Geochim. Cosmochim. Acta* **2016**, *181*, 36−53.

(51) Altmaier, M.; Gaona, X.; Fanghänel, T. Recent Advances in Aqueous Actinide Chemistry and Thermodynamics. *Chem. Rev.* **2013**, *113* (2), 901−943.

(52) Wheaton, V.; Majumdar, D.; Balasubramanian, K.; Chauffe, L.; Allen, P. G. A Comparative Theoretical Study of Uranyl Silicate Complexes. *Chem. Phys. Lett.* **2003**, *371* (3−4), 349−359.

(53) Novikov, A. P.; Kalmykov, S. N.; Utsunomiya, S.; Ewing, R. C.; Horreard, F.; Merkulov, A.; Clark, S. B.; Tkachev, V. V.; Myasoedov, B. F. Colloid Transport of Plutonium in the Far-Field of the Mayak Production Association, Russia. *Science (Washington, DC, U. S.)* **2006**, *314* (5799), 638−641.

(54) Utsunomiya, S.; Kersting, A. B.; Ewing, R. C. Groundwater Nanoparticles in the Far-Field at the Nevada Test Site: Mechanism for Radionuclide Transport. *Environ. Sci. Technol.* **2009**, *43* (5), 1293−1298.

(55) Dittrich, T. M.; Boukhalfa, H.; Ware, S. D.; Reimus, P. W. Laboratory Investigation of the Role of Desorption Kinetics on Americium Transport Associated with Bentonite Colloids. *J. Environ. Radioact.* **2015**, *148*, 170−182.

(56) Prescher, C.; Prakapenka, V. B. DIOPTAS: A Program for Reduction of Two-Dimensional X-Ray Diffraction Data and Data Exploration. *High Pressure Res.* **2015**, *35* (3), 223−230.

(57) Toby, B. H.; Von Dreele, R. B. GSAS-II: The Genesis of a Modern Open-Source All Purpose Crystallography Software Package. *J. Appl. Crystallogr.* **2013**, *46* (2), 544−549.

(58) Deng, B.; Ibers, J. A. Dicerium Disilicate, $Ce_2[Si_2O_7]$. *Acta Crystallogr., Sect. E: Struct. Rep. Online* **2005**, *61* (5), i76.

(59) Belokoneva, E. L.; Petrova, T. L.; Simonov, M. A.; Belov, N. V. Crystal-Structure of Synthetic TR-Analogs of Apatite $Dy_{4.67}(GeO_4)_3O$ and $Ce_{4.67}(SiO_4)_3O$. *Kristallografiya* **1972**, *17* (3), 429−431.

(60) Navrotsky, A. Progress and New Directions in Calorimetry: A 2014 Perspective. *J. Am. Ceram. Soc.* **2014**, *97* (11), 3349−3359.

(61) Guo, X.; Szenknect, S.; Mesbah, A.; Labs, S.; Clavier, N.; Poinssot, C.; Ushakov, S. V.; Curtius, H.; Bosbach, D.; Ewing, R. C.; Burns, P. C.; Dacheux, N.; Navrotsky, A. Thermodynamics of Formation of Coffinite, $USiO_4$. *Proc. Natl. Acad. Sci. U. S. A.* **2015**, *112* (21), 6551−6555.

(62) Helean, K. B.; Navrotsky, A.; Vance, E. R.; Carter, M. L.; Ebbinghaus, B.; Krikorian, O.; Lian, J.; Wang, L. M.; Catalano, J. G. Enthalpies of Formation of Ce-Pyrochlore, $Ca_{0.93}Ce_{1.00}Ti_{2.035}O_{7.00}$, U-Pyrochlore, $Ca_{1.46}U^{4+}{}_{0.23}U^{6+}{}_{0.46}Ti_{1.85}O_{7.00}$ and Gd-Pyrochlore, $Gd_2Ti_2O_7$: Three Materials Relevant to the Proposed Waste Form for Excess Weapons Plutonium. *J. Nucl. Mater.* **2002**, *303* (2−3), 226−239.

(63) Navrotsky, A.; Shvareva, T.; Guo, X. Thermodynamics of Uranium Minerals and Related Materials. In *Uranium—Cradle to*

Grave; Vol. *43*, Burns, P. C., Sigmon, G. E., Eds. Mineralogical Association of Canada: Winnipeg, Manitoba, Canada, 2013; pp 147−164.

(64) Guo, X.; Tiferet, E.; Qi, L.; Solomon, J. M.; Lanzirotti, A.; Newville, M.; Engelhard, M. H.; Kukkadapu, R. K.; Wu, D.; Ilton, E. S.; Asta, M.; Sutton, S. R.; Xu, H.; Navrotsky, A. U(v) in Metal Uranates: A Combined Experimental and Theoretical Study of $MgUO_4$, $CrUO_4$, and $FeUO_4$. *Dalt. Trans.* **2016**, *45* (11), 4622−4632.

(65) Guo, X.; Wu, D.; Xu, H.; Burns, P. C.; Navrotsky, A. Thermodynamic Studies of Studtite Thermal Decomposition Pathways via Amorphous Intermediates UO_3, U_2O_7, and UO_4. *J. Nucl. Mater.* **2016**, *478*, 158−163.

(66) Gorman-Lewis, D.; Mazeina, L.; Fein, J. B.; Szymanowski, J. E. S.; Burns, P. C.; Navrotsky, A. Thermodynamic Properties of Soddyite from Solubility and Calorimetry Measurements. *J. Chem. Thermodyn.* **2007**, *39* (4), 568−575.

(67) Bolech, M.; Janssen, F. J. J. G.; Booij, A. S.; Cordfunke, E. H. P. The Standard Molar Enthalpies of Formation of β-$La_2Si_2O_7$ and β-$Ce_2Si_2O_7$. *J. Chem. Thermodyn.* **1996**, *28* (11), 1319−1324.

(68) Shannon, R. D. Revised Effective Ionic Radii and Systematic Studies of Interatomic Distances in Halides and Chalcogenides. *Acta Crystallogr., Sect. A: Cryst. Phys., Diffr., Theor. Gen. Crystallogr.* **1976**, *32* (5), 751−767.

(69) Hosseini, S. M.; Navrotsky, A. Energetic Effects of Substitution of La-Nd and Si-Ge Oxyapatite-Type Materials. *J. Am. Ceram. Soc.* **2013**, *96* (12), 3915−3919.

(70) Hosseini, S. M.; Shvareva, T.; Navrotsky, A. Energetics of Lanthanum Silicate Apatite: Influence of Interstitial Oxygen and Cation Vacancy Concentrations in $La_{9.33+x}(SiO_4)_6O_{2+3x/2}$ and $La_{10\text{-}x}Sr_x(SiO_4)_6O_{3-0.5x}$. *Solid State Ionics* **2013**, *233*, 62−66.

(71) Ueno, S.; Jayaseelan, D. D.; Kita, H.; Ohji, T.; Lin, H. T. Comparison of Water Vapor Corrosion Behaviors of $Ln_2Si_2O_7$ (Ln = Yb and Lu) and $ASiO_4$ (A = Ti, Zr and Hf) EBC's. *Key Eng. Mater.* **2006**, *317−318*, 557−560.

(72) Garcia, E.; Sotelo-Mazon, O.; Poblano-Salas, C.A.; Trapaga, G.; Sampath, S. Characterization of $Yb_2Si_2O_7$−Yb_2SiO_5 Composite Environmental Barrier Coatings Resultant from in Situ Plasma Spray Processing. *Ceram. Int.* **2020**, *46*, 21328.

(73) Ding, Z.; Ridley, M.; Deijkers, J.; Liu, N.; Hoque, M. S. Bin; Gaskins, J.; Zebarjadi, M.; Hopkins, P.; Wadley, H.; Opila, E.; Esfarjani, K.; The Physical and Mechanical Properties of Hafnium Orthosilicate: Experiments and First-Principles Calculations. Preprint 2020.

(74) Nesse, W. D. *Introduction to Mineralogy*, 2nd ed.; Oxford University Press, 2000.

(75) West, A. *Solid State Chemistry and Its Application*; 2nd ed.; Wiley, 2014.

(76) Klemm, H. Silicon Nitride for High-Temperature Applications. *J. Am. Ceram. Soc.* **2010**, *93* (6), 1501−1522.

(77) Navrotsky, A. Systematic Trends and Prediction of Enthalpies of Formation of Refractory Lanthanide and Actinide Ternary Oxide Phases. *Ceram. Trans.* **2001**, No. 119, 137−146.

(78) Helean, K. B.; Navrotsky, A.; Lumpkin, G. R.; Colella, M.; Lian, J.; Ewing, R. C.; Ebbinghaus, B.; Catalano, J. G. Enthalpies of Formation of U-, Th-, Ce-Brannerite: Implications for Plutonium Immobilization. *J. Nucl. Mater.* **2003**, *320* (3), 231−244.

(79) Navrotsky, A. Thermochemical Insights into Refractory Ceramic Materials Based on Oxides with Large Tetravalent Cations. *J. Mater. Chem.* **2005**, *15* (19), 1883−1890.

(80) Qi, J.; Guo, X.; Mielewczyk-Gryn, A.; Navrotsky, A. Formation Enthalpies of $LaLnO_3$ (Ln = Ho, Er, Tm and Yb) Interlanthanide Perovskites. *J. Solid State Chem.* **2015**, *227*, 150−154.

(81) Helean, K. B.; Ushakov, S. V.; Brown, C. E.; Navrotsky, A.; Lian, J.; Ewing, R. C.; Farmer, J. M.; Boatner, L. A. Formation Enthalpies of Rare Earth Titanate Pyrochlores. *J. Solid State Chem.* **2004**, *177* (6), 1858−1866.

(82) Chen, F.; Ewing, R. C.; Clark, S. B. The Gibbs Free Energies and Enthalpies of Formation of U^{6+} Phases: An Empirical Method of Prediction. *Am. Mineral.* **1999**, *84* (4), 650−664.

(83) Sverjensky, D.; Shock, E. L.; Helgeson, H. C. Prediction of the Thermodynamic Properties of Aqueous Metal Complexes to 1000 C and 5 Kb. *Geochim. Cosmochim. Acta* **1997**, *61* (7), 1359−1412.

(84) Jenkins, H. D. B.; Glasser, L. Standard Absolute Entropy, $S°_{298}$, Values from Volume or Density. *Inorg. Chem.* **2003**, *42* (26), 8702−8708.

(85) Anderson, D. L.; Anderson, O. L. The Bulk Modulus-Volume Relationship for Oxides. *J. Geophys. Res.* **1970**, *75* (17), 3494−3500.

(86) Xu, H.; Zhao, Y.; Zhang, J.; Wang, Y.; Hickmott, D. D.; Daemen, L. L.; Hartl, M. A.; Wang, L. Anisotropic Elasticity of Jarosite: A High-P Synchrotron XRD Study. *Am. Mineral.* **2010**, *95* (1), 19−23.

(87) Glasser, L. Thermodynamics of Condensed Phases: Formula Unit Volume, V_m, and the Determination of the Number of Formula Units, Z, in a Crystallographic Unit Cell. *J. Chem. Educ.* **2011**, *88* (5), 581−585.

(88) Robie, R. A.; Hemingway, B. S. Thermodynamic Properties of Minerals and Related Substances at 298.15 K and 1 bar (105 Pascals) Pressure and at Higher Temperatures. *U.S. Geol. Surv. Bull.* **1995**, 2131.

(89) Strzelecki, A. C.; Bourgeois, C.; Kriegsman, K. W.; Estevenon, P.; Wei, N.; Szenknect, S.; Mesbah, A.; Wu, D.; Ewing, R. C.; Dacheux, N.; Guo, X. Role of Water and Hydroxyl Groups in the Structures of Stetindite and Coffinite, $MSiO_4$ (M= Ce, U). *Inorg. Chem.* **2020**, *59*, 13174.

(90) Guo, X.; Xu, H. Enthalpies of Formation of Polyhalite: A Mineral Relevant to Salt Repository. *J. Chem. Thermodyn.* **2017**, *114*, 44−47.

(91) Leitner, J.; Sedmidubsky, D.; Ruzicka, K.; Svobo, P. Calorimetric Determination of Heat Capacity, Entropy and Enthalpy of Mixed Oxides in the System CaO−SrO−Bi_2O_3−Nb_2O_5−Ta_2O_5. In *Applications of Calorimetry in a Wide Context - Differential Scanning Calorimetry, Isothermal Titration Calorimetry and Microcalorimetry*; Elkordy, A. A., Ed.; BoD − Books on Demand, 2013; pp 385−406.

(92) Bolech, M.; Cordfunke, E. H. P.; van Genderen, A. C. G.; Van Der Laan, R. R.; Janssen, F. J. J. G.; van Miltenburg, J. C. The Heat Capacity and Derived Thermodynamic Functions of $La_2Si_2O_7$ and $Ce_2Si_2O_7$ from 4 to 1000 K. *Thermochim. Acta* **1996**, *284* (96), 253−261.

(93) Ahlborg, N. L.; Zhu, D. Calcium-Magnesium Aluminosilicate (CMAS) Reactions and Degradation Mechanisms of Advanced Environmental Barrier Coatings. *Surf. Coat. Technol.* **2013**, *237*, 79−87.

(94) Costin, D. T.; Mesbah, A.; Clavier, N.; Dacheux, N.; Poinssot, C.; Szenknect, S.; Ravaux, J. How to Explain the Difficulties in the Coffinite Synthesis from the Study of Uranothorite? *Inorg. Chem.* **2011**, *50* (21), 11117−11126.

(95) Guo, X.; Szenknect, S.; Mesbah, A.; Clavier, N.; Poinssot, C.; Wu, D.; Xu, H.; Dacheux, N.; Ewing, R. C.; Navrotsky, A. Energetics of a Uranothorite ($Th_{1\text{-}X}U_XSiO_4$) Solid Solution. *Chem. Mater.* **2016**, *28* (19), 7117−7124.

(96) Costin, D. T.; Mesbah, A.; Clavier, N.; Szenknect, S.; Dacheux, N.; Poinssot, C.; Ravaux, J.; Brau, H. P. Preparation and Characterization of Synthetic $Th_{0.5}U_{0.5}SiO_4$ Uranothorite. *Prog. Nucl. Energy* **2012**, *57*, 155−160.

(97) Anderson, G. M.; Crerar, D. A. *Thermodynamics in Geochemistry: The Equilibrium Model*; Oxford University Press: New York, 1993.

(98) Miyawaki, R.; Yokoyama, K.; Husdal, T. A. Bastnäsite-(Nd), a New Nd-Dominant Member of the Bastnäsite Group from the Stetind Pegmatite, Tysfjord, Nordland, Norway. *Eur. J. Mineral.* **2013**, *25* (2), 187−191.

(99) Estevenon, P.; Welcomme, E.; Szenknect, S.; Mesbah, A.; Moisy, P.; Poinssot, C.; Dacheux, N. Preparation of $CeSiO_4$ from Aqueous Precursors under Soft Hydrothermal Conditions. *Dalt. Trans.* **2019**, *48* (22), 7551−7559.

(100) Taylor, S. R.; Mclennan, S. M. The Geochemical Evolution of the Continental Crust. *Rev. Geophys.* **1995**, *33* (2), 241−265.

(101) Wedepohl, K. H. The Composition of the Continental Crust. *Geochim. Cosmochim. Acta* **1995**, *59* (7), 1217−1232.

(102) Holtstam, D.; Andersson, U. B. The Ree Minerals Of The Bastnäs-Type Deposits, South-Central Sweden. *Can. Mineral.* **2007**, *45*, 1073−1114.

(103) Geijer, P. The Cerium Minerals of Bastnas at Riddarhyttan. *Sveriges Geol. Unders.* **1921**, *26*, 1−24.

(104) Lahti, S. I.; Suominen, V. Occurrence, Crystallography and Chemistry of the Fluocerite-Bastnaesite-Cerianite Intergrowth from the Fjälskär Granite, Southwestern Finland. *Bull. Geol. Soc. Finl.* **1988**, *60* (1), 45−53.

(105) Beukes, G. J.; De Bruiyn, H.; Van Der Westhuizen, W. A. Fluocerite and Associated Minerals from the Baviaanskranz Granite Pegmatite near Kakamas, South Africa. *South African J. Geol.* **1991**, *94* (4), 313−320.

(106) Chen, H.; Marcial, J.; Ahmadzadeh, M.; Patil, D.; McCloy, J. Partitioning of Rare Earths in Multiphase Nuclear Waste Glass-Ceramics. *Int. J. Appl. Glass Sci.* **2020**, *11*, 660.

(107) Urso, K.; Sridharan, K.; Jaques, B. J.; Alanko, G.; Butt, D. P.; Meyer, M.; Xu, P.; Tyburska-Paschel, B. High-Temperature Corrosion Testing of Uranium Silicide Surrogates. *Nucl. Technol.* **2016**, *196* (1), 100−110.

(108) Swift, P. N.; Bonano, E. J. Geological Disposal of Nuclear Waste in Tuff: Yucca Mountain (USA). *Elements* **2016**, *12* (4), 263−268.

(109) Hedin, A.; Olsson, O. Crystalline Rock as a Repository for Swedish Spent Nuclear Fuel. *Elements* **2016**, *12* (4), 247−252.

(110) Grambow, B. Geological Disposal of Radioactive Waste in Clay. *Elements* **2016**, *12* (4), 239−245.

(111) Krumhansl, J. L.; Papenguth, H. W.; Zhang, P. C.; Kelly, J. W.; Anderson, H. L.; Hardesty, J. O. E. Behavior of MgO as a CO2 Scavenger at the WIPP. *MRS Online Proc. Libr.* **1999**, *608*, 155−160.

(112) Choppin, G. R. Actinide Speciation in the Environment. *J. Radioanal. Nucl. Chem.* **2007**, *273* (3), 695−703.

(113) Cotton, S. *Lanthanide and Actinide Chemistry*; John Wiley & Sons, Ltd, 2006.

(114) Seaborg, G. T. Origin of the Actinide Concept. In Handbook on the Physics and Chemistry of Rare Earths; Gschneidner, K. A., Eyring, L. J., Choppin, G. R., Lander, G. H., Eds.; Elsevier B.V, 1994; Vol. *18*, pp 1−26.

(115) Seaborg, G. T. The Transuranium Elements. *Science* **1946**, *104* (2704), 379−386.

(116) Momma, K.; Izumi, F. VESTA 3 for Three-Dimensional Visualization of Crystal, Volumetric and Morphology Data. *J. Appl. Crystallogr.* **2011**, *44* (6), 1272−1276.

(117) Sawant, R. M.; Verma, P.; Mhatre, H. R.; Chaudhuri, N. K.; Ramakumar, K. L. Stability Constants of the Aqueous Mono-Fluoride Complexes of Pu(III) and Am(III) and Their Correlation with Other Metal Ions. *J. Radioanal. Nucl. Chem.* **2003**, *256* (3), 387−394.